# Organic Field Effect Transistors: Interfacial Modification, Dielectric Properties Control, and Semiconductor Molecular Design.

Daniel Orrin Hutchins

A thesis
submitted in partial fulfillment of the
requirements for the degree of

Master of Science in Materials Science and Engineering

University of Washington
2012

Committee:
Professor Hong Ma
Professor Marco Rolandi

Program Authorized to Offer Degree
Materials Science and Engineering

# ACKNOWLEDGEMENTS

Daniel Hutchins wishes to thank:

The faculty of the University of Washington Materials Science and Engineering Department for providing an unparalleled undergraduate and graduate education.

Professors Alex K.Y. Jen and Hong Ma, for providing academic guidance, research funding, and state of the art lab facilities.

My family, for continued support of my academic endeavors.

All members of the Jen Group past and present for making the late nights and long hours more enjoyable. Special thanks to Orb Acton and Nathan Cernetic.

Thank you!

University of Washington

## Abstract

# Organic Field Effect Transistors: Interfacial Modification, Dielectric Properties Control, and Semiconductor Molecular Design.

Daniel Orrin Hutchins

Chair of the Supervisory Committee:

Professor Hong Ma

Materials Science and Engineering

In recent years, organic electronics have become a field of interest in both academic and industrial settings. Through the integration of semiconducting organic small molecules/polymers into existing device architectures low cost, flexible, solution processed, circuitry can be achieved. Specifically, high performance organic field effect transistors (OFETs) facilitate the construction of background logic to active matrix displays, RFID cards, chemical sensors, and a method of testing intrinsic electronic properties of organic materials. Due to their potential for ubiquitous use, device performance in a variety of applications must be optimized. In this thesis, methods to enhance performance of OFET devices will be discussed with respect to semiconductor-dielectric interfacial modification, dielectric properties control, and semiconductor molecular design. These three tenants governing OFET device performance are explored through experiments in self-assembly, synthetic chemistry and dielectric alteration.

# TABLE OF CONTENTS

**Page**

## LIST OF FIGURES

**Figure Number** **Page**

# LIST OF TABLES

**Figure Number** **Page**

# Introduction to Organic Electronics

Following discovery of the first semiconducting polymer, doped polyacetalene, by Heeger, MacDiarmid, and Shirakawa in 1977, the use of π-conjugated small molecules/polymers for electronics applications has become a hot topic in industrial and academic settings.[1-3] Several dominant fields of research have emerged as a result: organic field effect transistors (OFET), organic photovoltaic devices (OPV), and organic light emitting diodes (OLED).[4-6] By modifying classical semiconducting device architectures, organic materials can be used to replace conventional inorganic components facilitating some forms of increased functionality such as flexibility, low cost devices, vacuum free processing, and low temperature processing.[7-9] Despite the advantages conferred by organic materials, fundamental limitations such as low charge carrier mobility and ease of degradation have slowed integration of these technologies into commercial products.[10]

Unlike inorganic covalently bound semiconductors, in which charge transport occurs through band-like transport mechanisms, organic structures are Van der Waals bound and conduct charge as a result of "electron/hole hopping" between molecules.[11] In this process an activation energy must be overcome for charge transport to occur, resulting in slowed $e^-/h^+$ flow through the semiconducting media. Despite this, electronic properties of organic materials are still governed by quantum mechanical phenomena; analogous to those exhibited by inorganic semiconductors.[12]

The simplest description of organic band theory is illustrated through examination of the covalent bond between diatomic hydrogen which possesses just two permutations of the wave function (bonding and antibonding orbitals). As the system must obey the Poly Exclusion Principal (PEP), in which no two fermions can exist with the same sign spin in any one atomic orbital, three possible states exist. (1) The ground (boding) state where the two electrons are in their lowest energy state, one with spin +1/2 and the other with spin -1/2. (2) The first anibonding state in which one electron populates the bonding state and the other populates the antibonding state (as there is no conflict with the PEP these can have any sign spin). (3) The second antibonding state where both electrons are spin +1/2 -1/2 in the antibonding orbital. Although the aforementioned is a description of the most basic covalently bonded molecule, this model can be extrapolated to larger systems. As molecular structures incorporate more atoms and a greater number of bonds, bonding/anti-bonding states increase proportionally. As the size of the structure grows, electronic states with similar energy levels begin to be tightly grouped, eventually forming an electronic density of states similar to that of an inorganic material.[12, 13] The energy levels associated with the highest-energy bonding state and the lowest-energy anti-bonding state are termed "highest occupied molecular orbital" (HOMO) and "lowest unoccupied molecular orbital" (LUMO). These energy levels are analogous to the valiance and conduction (respectively) bands in inorganic structures.[6, 14]

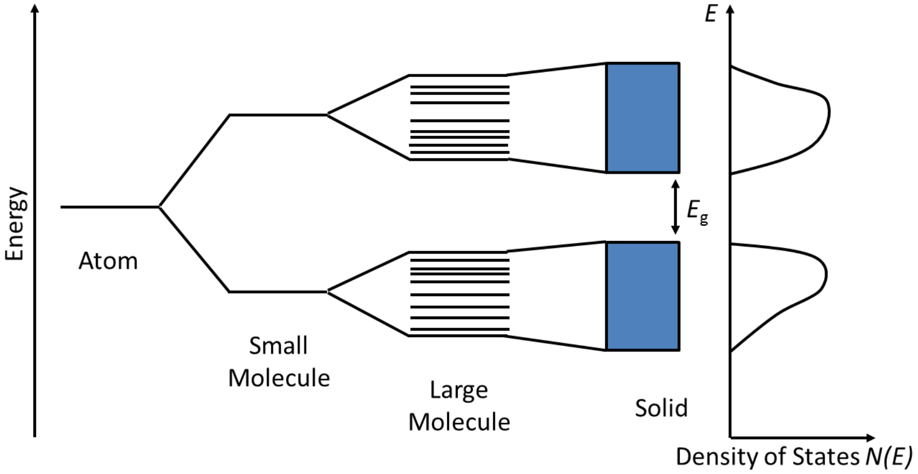

**Figure 1.** Visual schematic of bonding/anti-bonding state coalescence with increasing molecular size. As the number of atoms in a molecular system grow, so does the number of available states.

For device fabrication of all types, knowledge of LUMO/HOMO energy level location is paramount to achieving an optimized architecture. Efficient change injection/extraction to/from electrodes can only be achieved through Ohmic contact with the semiconductor.[15] This occurs when the work function of the electrode aligns with the LUMO/HOMO value of the organic semiconductor. Additionally, in OPV and OLED devices charge transfer through the active layer is efficient only if energy levels of both n/p-type semiconductors are aligned relative to each other.[16]

Although all three device types are worth mentioning, as the solid state physics governing operation is similar in many ways, the remainder of this paper will be devoted to the discussion of OFETs.

## Organic Field Effect Transistors

Organic field effect transistors (OFETs) have become the subject of intense research due to the appeal of inexpensive, solution processed, and mechanically flexible electronic devices. Possible applications include radio frequency identification tags, smart cards, and drivers for active matrix displays.[7, 10, 17-19] By using π-conjugated organic materials as semiconductors, flexible devices can be achieved with reel to reel processing techniques.[20] In research applications, FET devices allow for simple electronic properties measurements to be made; charge carrier mobility values can be easily extracted from new semiconductors with three terminal measurements along with other FET figures of merit. [21]

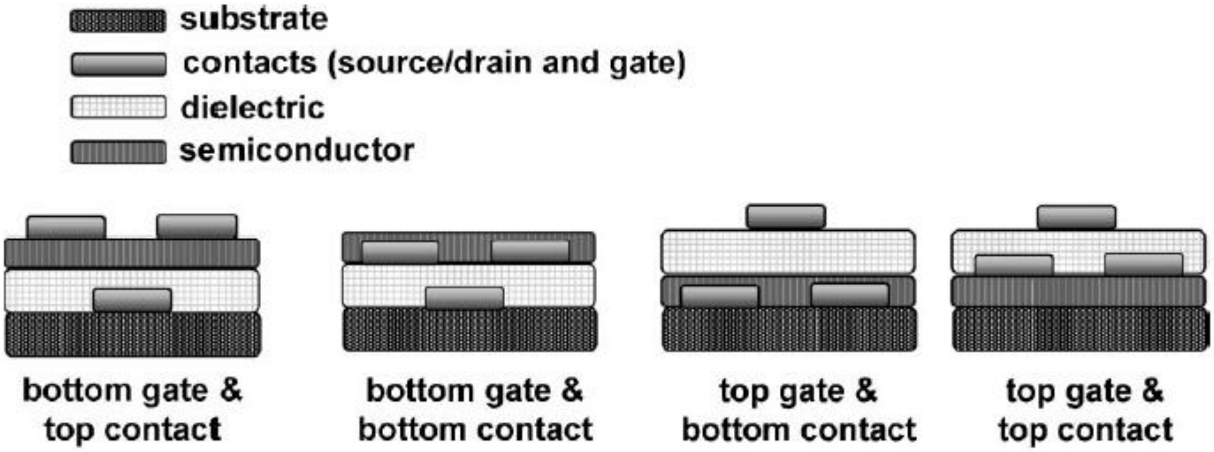

**Figure 2.** Possible permutations of OFET device architecture. Reproduced from Ref. 22.

The transistor, best described as a voltage controlled current switch, is the most fundamental piece of digital logic.[11] The basic architectures of organic FET devices are illustrated in **Fig 2**. Although differences between structures can be seen, it should be noted that all possess a gate electrode separated from the semiconductor by an insulated layer.[17] Additionally, the semiconductor has two electrodes in direct contact with it (source and drain). By applying a source to gate (electrode not in contact with semiconductor) voltage, charge accumulates at the semiconductor dielectric interface. With a source to drain voltage of the same sign, current flow is realized. Using this current-on-current-off functionality, binary logic can be achieved, creating the 1/ 0 scheme commonly associated with digital technology.[17]

Basic OFET performance is governed by the equations:

$$(I_{\mathrm{SD}})_{\mathrm{lin}} = \left(\frac{W}{L}\right)\mu C\left(V_{\mathrm{G}} - V_{\mathrm{T}} - \frac{V_{\mathrm{SD}}}{2}\right)V_{\mathrm{SD}} \qquad (1)$$

$$(I_{\mathrm{SD}})_{\mathrm{sat}} = \left(\frac{W}{2L}\right)\mu C(V_{\mathrm{G}} - V_{\mathrm{T}})^2 \qquad (2)$$

where both I terms represent source to drain current in either the linear or saturation regimes, μ is electron/hole mobility of the semiconductor, L the channel length, W channel width, C dielectric capacitance per unit area, $V_T$ threshold voltage, $V_G$ gate voltage, and $V_{SD}$ drain voltage.[17] From these two equations it should be noted that there are two structural parameters for increasing "on" current flow through the device (aside from altering electrode geometry or applying larger voltages): Higher-mobility semiconductors can be used and dielectric capacitance can be increased. These areas of device engineering comprise two of the most basic aspects of OFET design.[23]

As capacitance is given by $C = (\varepsilon_o k)/d$, where C is capacitance per unit area, $\varepsilon_o$ is the permeability of free space, k is dielectric constant, and d is distance, dielectric media are frequently designed to increase resulting FET device properties.[24] By decreasing dielectric thickness, larger electric fields are able to be imparted on the semiconductor; however, smaller thicknesses allow for greater leakage current and lower breakdown voltages.[25] Additionally, by increasing the value of the dielectric constant, polarizability of the dielectric increases; once again resulting in larger electric fields. Classically, this has been accomplished using metal oxides with large electronegativity differences between cation and anion (such as hafnium oxide or zirconium oxide).[19] However, with this increased polarizablity comes impeded semiconductor transport properties due to coupling of charge carriers and dielectric phonons.[26]

# Modern OFET Technology

Since the advent of semiconducting polymers many advances have been made in materials and processing to facilitate the construction of high performance FET devices.[27, 28] Not only have the intrinsic properties of the semiconducting molecules improved, but also other aspects of device engineering that prove to be equally influential in governing OFET performance. [29]

As several thousand organic electronics manuscripts have been published since 1977, a quick review will be given showcasing some recent influential papers and their role in directing the modern OFET field of research.

### State of the Art Interfacial Modification

Although not intrinsic to the equations governing OFET performance, it has become a staple of organic electronic technologies that proper treatment of interfaces can influence device performance as much as semiconductor molecular design.[17, 30] Blocking of charge traps at the semiconductor dielectric interface can improve mobility measurements several orders in magnitude as well as allow classically P-type materials to conduct electrons.[27] As charge transport occurs in the first few molecular layers of semiconductor, surface species drastically impact device performance. Charge trapping sites typically are the product of (-OH) groups on the surface of inorganic oxides and greatly impede the flow of charge carriers through the semiconductor.

### *Insulating Polymers*

One manuscript demonstrating the highly critical nature of interfacial modification was published by Chua *et al.* using divinyltetramethylsiloxane-bis(benzocyclobutene) (BCB) as a dielectric material.[31] BCB is thermally cross-linkable polymer developed by the DuPont company which provides an ideal surface for OFET device construction because of its charge trap blocking properties and ultra-smooth surface. Through the use of a BCB dielectric, semiconducting polymers typically regarded as P-type were shown to demonstrate N-type behavior. Additionally, mobility measurements achieved were high in comparison to previously reported values for these structures. This paper put forth the now commonly held notion that a properly chosen dielectric/semiconductor interface is just as influential as the molecular design of the semiconductor in maximizing device performance.

### *Self-Assembled Monolayers*

Although polymer dielectrics offer potential as the insulator of choice for organic materials, self-assembled monolayers SAMs provide another attractive option for dielectric modification.[32] SAMs are single molecular layers chemically adhered to substrate surfaces.[33] As inorganic electronics have used transition metal oxides as the dielectric material of choice for the last 50 years, integration of these materials into OFET devices is highly desirable.[34] However, despite their robust insulating properties, the surface of inorganic oxides are saturated with surface hydroxyl groups.[35] To mitigate the effects of this property, SAMs are commonly used. Despite their miniscule thickness, SAMs not only provide a transitional layer between inorganic oxide and organic semiconductor but can function as a low voltage dielectric if properly designed.[36]

Five types of SAM binding chemistries persist in organic electronics literature, each with their own distinct use cases. Alkyl-thiol based SAM structures are the most well studied and provide a basis to which all other forms of self-assembly are compared. Seminal works by Whitesides *et al.* using thiols in biological applications date back several decades and still act as the standard for many self-assembly experiments.[37] Despite their well-studied nature, biding is limited to noble metals and some semiconducting elements. Physiabsorbed molecules can also be used to form SAMs, however, due to the lack of chemical binding, structures possess little resilience to mechanical forces and assembly conditions are difficult to control.[38] Carboxilic acids have been used to form bonds with metal oxides, however, there reactivity is limited and achieving dense assembly can be problematic.[39] Silane based molecules readily react with many inorganic oxides including $SiO_2$ and are frequently used to aid in lithographic processes on Si wafers. Despite their frequent use, several problems persist because of their high reactivity; molecules are unstable in the presence of moisture, have the propensity to homocondense, and require highly controlled reaction conditions to prevent multilayer/molecular agglomeration on substrate surfaces.[40] Due to these drawbacks associated with other forms of self-assembly binding chemistries, phosphonic acids have risen to prominence because of their reactivity with a wide range of metal oxides, inability to homocondese and ambient stability.[39, 41]

Manuscripts demonstrating the use of SAMs for dielectric modification are numerous, however, not until recently has the SAM/semiconductor structure relationship been explored systematically.[42] This recent push for fundamental examination of SAM molecular structure and semiconductor performance has led to great advances in SAM technologies and trends in molecular design being established.

This is best illustrated in the paper by Kenjiro *et al.* in which chain length of alkyl-SAMs is evaluated with respect to FET device performance.[42] It was found that alkyl-chains of mid length ~$(CH_2)_{12}$ facilitate the highest mobility pentacene devices. This was attributed to the disordered nature of mid-length alkyl chain SAMs promoting a smooth liquid like surface for semiconductor growth. Additionally, other manuscripts have shown that by using SAM terminal group structures complementary to that of the employed semiconductor, nucleation, growth, and morphology can be systematically controlled through molecular design.[43]

## Dielectric Properties Control

Associated with dielectric modification, is control of dielectric properties. Although one dominant mechanism of improving device performance has already been discussed through the blocking of charge traps, other design criteria facilitate similar goals.[44] Dielectric constant ($k$) can both enhance and detract from FET device performance. As $k$ value represents the magnitude of electric field applied to the semiconductor as a product of source to gate voltage, this can allow for higher source to drain currents.[45] Conversely, because dielectric constant is related to the polarizability of the dielectric, at high values Frohlich polaron formation can lead to a departure from the theoretical charge carrier mobility of the organic semiconductor of choice. This relationship was first explored by Hulea *et al.* and proves to be a guide when choosing a dielectric material for OFET applications. [26]

### *Ionic Gels*

Additionally, the use of ionic dielectric materials, in which a charged species is free to move through the dielectric medium under applied electric field, has allowed for the fabrication of OFETs exceeding performance figures of merit of comparable devices by several orders of magnitude. The use of ionic gel dielectrics in OFET devices was demonstrated by Panzer *et. al* and shows single digit mobility values for common OPV polymers such as P3HT, PQT-12, and F8T2.[46]

## Semiconductor Molecular Design

Though choice of dielectric and interfacial modification can have profound effects on device performance; semiconductor design ultimately limits operation parameters. Currently research efforts are focused on the design of soluble low band gap acceptor polymers, and n-type materials.

As of late, the best low band gap polymeric materials have been achieved using a weak-donor strong-acceptor structure, in which electron rich and electron deficient moieties are placed in complementary locations along the length of the chain. This donor acceptor structure facilitates a planar orientation of the polymer backbone subsequently resulting in greater π-electron delocalization and a lower band-gap.[47]

In addition to the development of low band gap polymeric materials, n-type organic semiconductors are another major focus of research efforts as these types of structures frequently exhibit lower charge carrier mobilities than their P-type counterparts.[18,48] This reduced performance hinders the advancement of OFET and OPV devices. Lagging n-type material properties is partially due to the relatively unsuccessful alteration of $C_{60}$-$C_{70}$ structures, as modification to the conventional PCBM side chain has resulted in decreases in semiconductor crystalinity/mobility.[48] Also related to this is the limited number of structures discovered that have better or equivalent LUMO energy values, ambient stability, and optimal level of crystalinity as $C_{60}$/$C_{70}$-PCBM.[49, 50] For OFET devices this small selection of n-type materials means difficulty in fabricating efficient complementary logic as both N and P-type FET devices with similar threshold voltage/mobility values are required.[51]

# Advancing OFET Technology: Thesis Projects

During my time in the Jen Group, my research efforts were devoted to the following three areas of OFET design: interfacial modification, dielectric properties control, and semiconductor molecular design. The remainder of the thesis will summarize the primary advances made with respect to the aforementioned three fields.

## Effect of Self-Assembled Monolayer Structural Order, Surface Homogeneity and Surface Energy on Pentacene Morphology and Thin Film Transistor Device Performance

As current flow in OFET devices occurs in the first few nanometers of the semiconductor,[52] a dielectric interface compatible with the semiconductor of choice is essential for optimized device performance. Due to the robust nature of high-*k* inorganic oxides and their established history in inorganic chipsets, integration of these materials into OFET devices has gained considerable attention.[39] However, the surfaces of these dielectric structures post fabrication are commonly saturated with –OH groups leading to non-negligible charge trapping effects in organic devices fabricated on this unmodified layer.[39] One proven method to block charge traps and provide a smooth transition from inorganic dielectric material to organic semiconductor is through the use of self-assembly.[40] Self-assembled monolayers (SAMs) are single molecular layers chemically adhered to a substrate surface and are frequently used in organic electronics to modify inorganic components of organic devices.[53] SAMs are particularly attractive for the small amount of material consumption necessary for complete monolayer formation, tunable structure/functionality through synthetic chemical processes, and ease of integration into processing lines through dip/spin casting onto preexisting oxide dielectric architectures.[54]

In the past few years, great effort has been devoted to exploring the relationship between SAM structure and electronic performance of various commonly used organic semiconducting small molecules/polymers. Mechanisms for improving device performance have included: surface energy, SAM density/phase states, and π-π and/or π-σ interactions.[55-57] However, these claims are frequently made using a narrow selection of SAM structures, leading to explanations that often correlate semiconductor performance to an observed trend without identifying a causal relationship. Additionally, results are sometimes achieved in conjunction with one or more confounding variables such as a large dielectric surface roughness or molecular aggregate on the SAM surface. Due to the breadth of mechanisms observed for SAM structure affecting device performance, our group chose to examine six SAM structures and their impact on pentacene device performance with respect to surface energy, surface homogeneity, and level of structural order; three underlying principles of SAM surface science. SAM molecules employed in this study were strategically designed to retain similarity to other molecules used with respect to one of the above principals, yet differ in another key aspect, in order to differentiate cause from correlation (ex. BA-11-PA, 12-PD-PA and  DDPA are all similar with respect to alkyl-chain length but have very different surface energy values).

Pentacene, an organic semiconducting molecule ubiquitous in OTFT literature, was chosen as the semiconductor in these experiments to examine the effect of monolayer structure on device performance as its "typical" values are well reported.[36, 58] Additionally, the conditions for its deposition are established and thermal evaporation is highly controllable; allowing for reproducible device performance and mitigation of undesired variables. It is important to note that though there have been some reports of extremely high mobility thin film pentacene measurements using unconventional dielectric platforms that are difficult to integrate into assembly line processes, most reported pentacene OFETs achieve charge carrier mobilities of 1.0 $cm^2\ V^{-1}\ s^{-1}$ if dielectric surfaces are properly modified.[59] Although, pentacene was specifically chosen for these studies, results obtained are directly applicable to other planar organic semiconducting compounds.

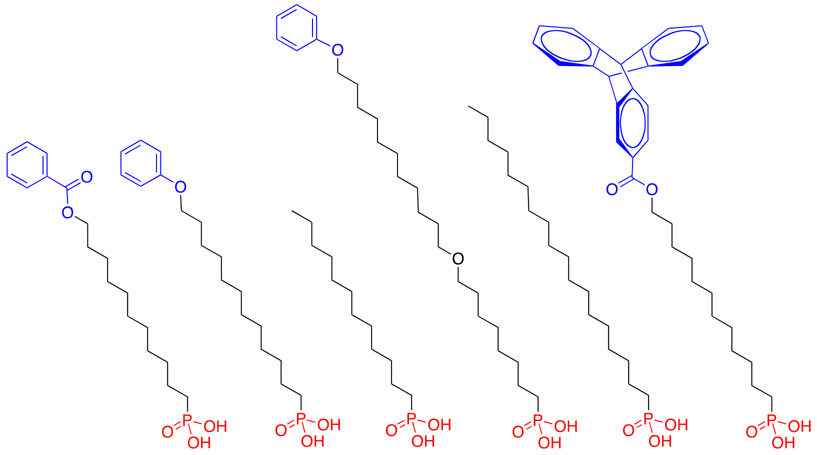

1 2 3 4 5 6

**Figure 3.** Molecular structures of all six SAMs used in this study. 1) Benzoic acid 11-phosphono-undecyl ester (BA-11-PA), 2) (12-Phenoxy-dodecyl)-phosphonic acid (12-PD-PA), 3) Dodecyl-phosphonic acid (DDPA), 4) [8-(11-Phenoxy-undecyloxy)-octyl]-phosphonic acid (PhO-19-PA), 5) Octadecyl-phosphonic acid (ODPA), and 6) 12-(2-triptycenylcarboxy)dodecylphosphonic acid (Trip-12-PA).

To elicit a true structure-property relationship between SAM structure and device performance, a dielectric platform must be carefully chosen to eliminate effects of extraneous variables such as surface roughness, Frolic polaron formation, and sites of nucleation such as grain boundaries. For these reasons our dielectric layer was chosen to be 300 nm thermally grown silicon oxide (0.2 nm RMS roughness) on a P-doped Si wafer. To promote binding of PA

SAMs, a 2-nm $AlO_x$ layer was deposited on the surface of the $SiO_2$ via a plasma enhanced deposition process. This dielectric platform has been extensively studied in our group and is an excellent way to research PA assembly as the surface post-$AlO_x$ plasma deposition is continuous, morphologically identical to the underlying Si, and readily reactive with PA in ambient conditions.[52, 53] Using this basic architecture, the following PA SAM molecules were chosen to study pentacene devices: Benzoic acid 11-phosphono-undecyl ester (BA-11-PA), (12-Phenoxy-dodecyl)-phosphonic acid (12-PD-PA), Dodecyl-phosphonic acid (DDPA), [8-(11-Phenoxy-undecyloxy)-octyl]-phosphonic acid (PhO-19-PA), Octadecyl-phosphonic acid (ODPA), and 12-(2-triptycenylcarboxy)dodecylphosphonic acid (Trip-12-PA) (**Fig. 3**). From systematic examination of the SAM structure – pentacene properties relationship, we propose dominant mechanisms for optimal pentacene grain growth and charge transport properties.

As previously stated, all SAM molecules were rationally designed to probe specific aspects of monolayer structure, surface homogeneity, and surface energy. BA-11-PA contains an alkyl-chain of $(CH_2)_{11,}$ to promote a disordered SAM structure, joined to a phenyl-ring by ester linkage for mid-level surface energy. 12-PD-PA SAM was similarly designed with $(CH_2)_{12}$ alkyl chain, however, is joined to its phenyl terminal group with an ether linkage to lower surface energy relative to BA-11-PA. DDPA SAM was chosen for its mid-length disordered alkyl chain (similar to BA-11-PA and DD12-PA), and low surface energy. PhO-19-PA SAM was selected for its comparable surface energy to 12-PD-PA, yet highly ordered and crystalline monolayer. ODPA SAM was chosen for its low surface energy, comparable to DDPA, and its well-ordered monolayer. Trip-12-PA SAM was specifically designed to be amorphous/disordered because of its mid length $(CH_2)_{12}$ alkyl chain, yet also have comparable surface energy to BA-11-PA.

However, unlike all of the other molecules, Trip-12-PA has a large pointed three-dimensional terminal groups chosen for its ability to form a SAM surface that is "molecularly rough."

**Table 1.** Advancing contact angle and surface energy data for SAM surfaces. Surface energy was calculated by the Wu (harmonic mean) method. DI $H_2O$ and diiodomethane (DIM) were used as probe solvents. The average of five advancing contact angle measurements is presented in the table with deviation less than 3° on any SAM surface. $\gamma_{polar}$ and $\gamma_{dispersive}$ were calculated from averaged contact angle measurements and summed to obtain $\gamma_{total}$.

| SAM | Avg. θ Water [°] | Avg. θ DIM [°] | $\gamma_{polar}$ [$mNm^{-1}$] | $\gamma_{dispersive}$ [$mNm^{-1}$] | $\gamma_{total}$ [$mNm^{-1}$] |
|---|---|---|---|---|---|
| BA-11-PA | 69.2 | 33.6 | 12.7 | 43.0 | 55.7 |
| 12-PD-PA | 82.0 | 38.6 | 7.5 | 40.8 | 48.3 |
| DDPA | 107.1 | 69.4 | 1.1 | 25.8 | 26.8 |
| PhO-19-PA | 79.7 | 38.1 | 8.4 | 41.0 | 49.4 |
| ODPA | 110.3 | 69.1 | 0.03 | 26.0 | 26.1 |
| Trip-12-PA | 68.8 | 37.1 | 13.2 | 41.5 | 54.6 |
| Bare $AlO_x$ | 12.0 | 36.5 | 37.7 | 41.7 | 79.4 |

Surface energy of all SAMs was measured via contact angle goniometry using the Wu model (harmonic mean) to calculate both dispersive ($\gamma^d$) and polar ($\gamma^p$) components of total surface energy ($\gamma^{total}$) (**Table 1**).[60] It should be noticed that many of the molecules in this study were designed to have similar surface energies but different structural order once assembled. Both alkyl-PA monolayers of DDPA and ODPA have similar and exceptionally low surface energies relative to the other SAM structures but have different alkyl-chain lengths. Similarly, PhO-19-PA and 12-PD-PA SAMs have comparable (although higher) surface energy values to each other, yet differ greatly in chain length. BA-11-PA SAM exhibits a slightly higher surface energy still, but is comparable in structure to 12-PD-PA. The triptycene-based SAM of Trip-12-

PA exhibits similar surface energy to BA-11-PA but differs in molecular-scale surface homogeneity due to the presence of a large three-dimensional terminal moiety.

AFM images obtained of these monolayers show SAM coated surfaces that are almost morphologically identical. No boundaries or defects can be resolved in the images and all substrates have a very similar surface roughness of 0.25-0.30 nm RMS, which is comparable to that of bare $SiO_2$.

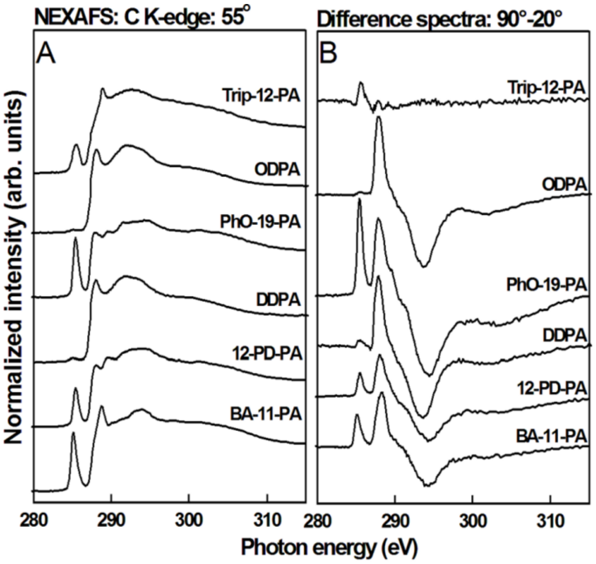

**Figure 4.** Near-edge X-ray absorption fine structure (NEXAFS) spectra taken of all SAMs used in this study. (A) Carbon K-edge spectra collected at 55° and (B) 90°-20° difference spectra.

**Table 2** Summary of NEXAFS-determined structural information

| | Δ*N* Chain | Δ*N* Phenyl |
|---|---|---|
| BA-11-PA | 0.35 | 0.10 |
| 12-PD-PA | 0.31 | 0.14 |
| DDPA | 0.29 | --[a] |
| PhO-19-PA | 0.41 | 0.30 |
| ODPA | 0.39 | -- |
| Trip-12-PA | -0.01 | 0.11 |

[a] not applicable.

Structural characterization of the SAM molecules adhered to the $AlO_x$ coated substrate was carried out through near edge X-ray absorption fine structure spectroscopy, yielding both a qualitative assessment of structural order and average tilt angle associated with various moieties. C *K*-edge spectra of the PA SAMs, collected at an X-ray incidence angle of 55°, can be found in **Fig. 4**. At an incident angle of 55°, the spectra are independent of orientation effects (the so-called magic angle of NEXAFS).[61] All spectra show characteristic absorption resonances at ~287.7 eV (R*/C–H σ*), and ~293.3 eV related to the aliphatic carbon chains (C–C σ*).[61] Trip-12-PA, PhO-19-PA, BA-11-PA and 12-PD-PA show an additional pronounced pre-edge feature near 285 eV associated with the terminal aromatic rings (C=C π*). Trip-12-PA and BA-11-PA also exhibit a C 1s – C=O resonance near 288.5 eV related to the ester moieties. For the other SAMs, no features related to C=O containing species – contaminants often found in SAMs.

NEXAFS difference spectra for 90° and 20° X-ray incidence angles can be found in the left panel of **Fig. 4**. The Trip-12-PA SAMs showed almost no dichroism and the film is mostly disordered. We will exclude Trip-12-PA from the following discussion of structural parameters. All other SAMs showed an angle dependence (i.e. difference spectra intensity) for the C–H and C–C related peaks, a clear indication that a well-defined monolayer-layer was formed. Molecular orbitals related to the R* transition (C–H) are oriented perpendicular to the alkyl chain axis while those related to transitions into the C–C and C–C’ σ* orbitals are oriented parallel to the chain axis. The polarity of the difference peaks thus proves the alkane chains are in an upright orientation. The π* resonances of BA-12-PA, 12-PD-PA and PhO-19-PA exhibited positive dichroisms signifying upright phenyl ring orientations.

For a more quantitative picture of the general PA SAM structure on $AlO_x$, the tilt angle of the *n*-alkyl chains and the ring structures for the most ordered SAM, PhO-19-PA, was determined from the dichroisms at the $R^*$ and $\pi^*$ resonances, respectively. The intensities of these resonances as a function of the X-ray incidence angle are evaluated for spectra collected at 90°, 70°, 55°, 30° and 20° using published procedures.[61] From this data the average tilt angle was found to be 27°± 5.0° for the alkyl chain and 66°±5.0° for the plane normal of the phenyl ring against the surface normal. This is in good agreement with the chain orientation found for PA SAMs on $HfO_x$, Ag and $SiO_x$.

Differences in SAM order and alignment were quantified by analyzing the NEXAFS dichroic ratio:

$$\Delta N = \frac{N_{90^\circ} - N_{20^\circ}}{N_{90^\circ} + N_{20^\circ}} \qquad (1)$$

where $N$ are the NEXAFS intensities recorded for a specific resonance in the 90° and 20° spectra. The SAM $\Delta N$ values for the alkane chains (C–H $\sigma^*$) and the terminal phenyl groups (C=C $\pi^*$) are summarized in **Table 2**.[62] For the chain order, there is a clear increase in molecular alignment going from shorter to longer alkane chains, the $\Delta N$ values increase by nearly 25% for the long-chain SAMs. The chain order also has significant impact on the alignment of the terminal groups. For the phenyl moieties the order parameter $\Delta N$ increases threefold going from any short-chain SAMs with mostly disordered phenyl units to the long-chain PhO-19-PA film with a $\Delta N$ of 0.30. In conclusion, while most SAMs studied here are generally well-defined films with a mostly upright orientation of the alkane and phenyl units, the order of the films was strongly dependent on the chain length. Shorter chains lead to a more disordered amorphous SAM structure, due to defects in the alkyl-chains.

To simplify interpretation of this data, SAMs used in this study are arranged into three groups based on alkyl-chain dichroic ratio: disordered (Trip-12-PA), less ordered (BA-11-PA, 12-PD-PA, DDPA), and more ordered (ODPA, PhO-19-PA). This will become important when discussing the relationship between SAM structure and device performance (**Scheme 1**).

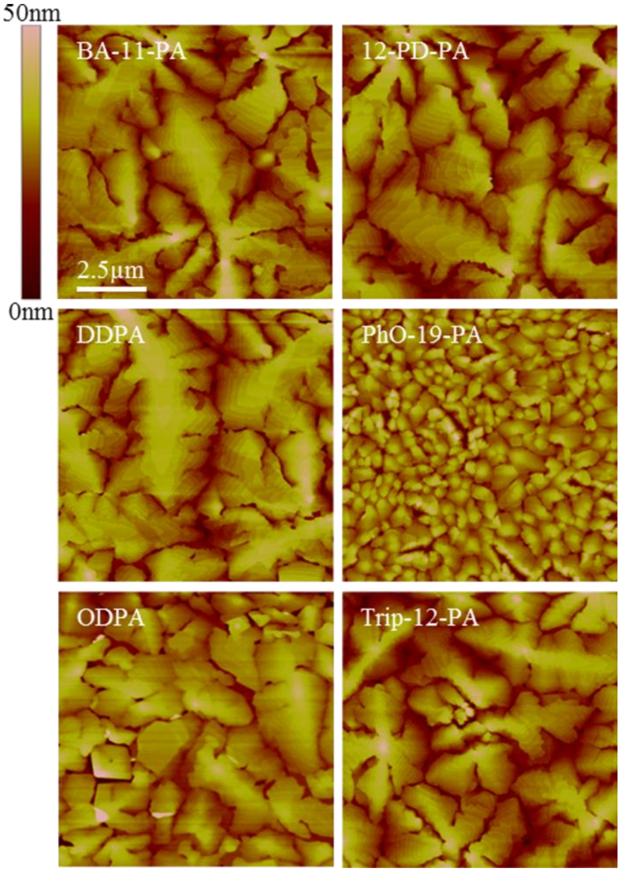

**Figure 5.** AFM images of 40 nm thick pentacene films evaporated on SAM surfaces. Large dendritic grains can be seen on SAMs of BA-11-PA, 12-PD-PA, and DDPA, relative to the other three SAMs.

Pentacene was thermally evaporated onto the SAM coated substrate surfaces to form the organic semiconducting layer of OFET device architectures. High mobility pentacene OFETs are typically characterized by large interdigitated dendritic crystals.[63] In **Fig. 5** the largest pentacene grains of this type are exhibited by SAMs of BA-11-PA, PD-12-PA and DDPA. Conversely, pentacene films grown on SAMs comprised of long alkyl chains ~$(CH_2)_{18}$ or longer are shown to have small boxy grains.[54] Although the triptycene-based SAM has roughly the same alkyl chain length as BA-11-PA, 12-PD-PA and DDPA, observed pentacene grain size is much smaller than any of these structures.

Nucleation and growth kinetics of monolayer pentacene can be used to explain the morphology seen in **Fig. 5**. It is known that the nucleation density of adsorbed pentacene molecules (N) is proportional to deposition rate (F) divided by surface diffusion constant (D): $N \approx F/D$. As F is held at 0.2 Å $s^{-1}$, the diffusion constant governs the growth process.[64] For alkyl-SAMs of length $\geq (CH_2)_{16}$ monolayers exhibit a highly ordered crystalline structure in which bonds are in an all trans-conformation. During the self-assembly process, grains between regions of highly ordered SAM are formed. This results in monolayer grain boundary defects on the surface acting as sites of pentacene nucleation; decreasing the surface diffusion constant and increase nucleation density. Mid-length disordered alkyl-SAM surface morphology can be compared to a liquid, reducing the impact of SAM grain boundaries. This eliminates potential sites for pentacene nucleation and decreases nucleation density.

SAMs of BA-11-PA and PD-12-PA facilitate large pentacene grain growth through this liquid-like surface mechanism, as pentacene thin films on these molecular structures are observed to have similar grain size and structure to that of DDPA. This demonstrates that the SAM terminal moiety has a degree of synthetic flexibility, and allows for tunable surface energy without compromising device performance. PhO-19-PA and ODPA SAM surfaces exhibit much smaller pentacene grain growth constant with the SAM grain boundary mechanism. Trip-12-PA SAM has liquid-like/disordered surface but results in small pentacene grain structure. Though this may seem counterintuitive, further explanation will be given in section the section entitled *"Pentacene Device Performance and SAM Surface Homogeneity Relationship."*

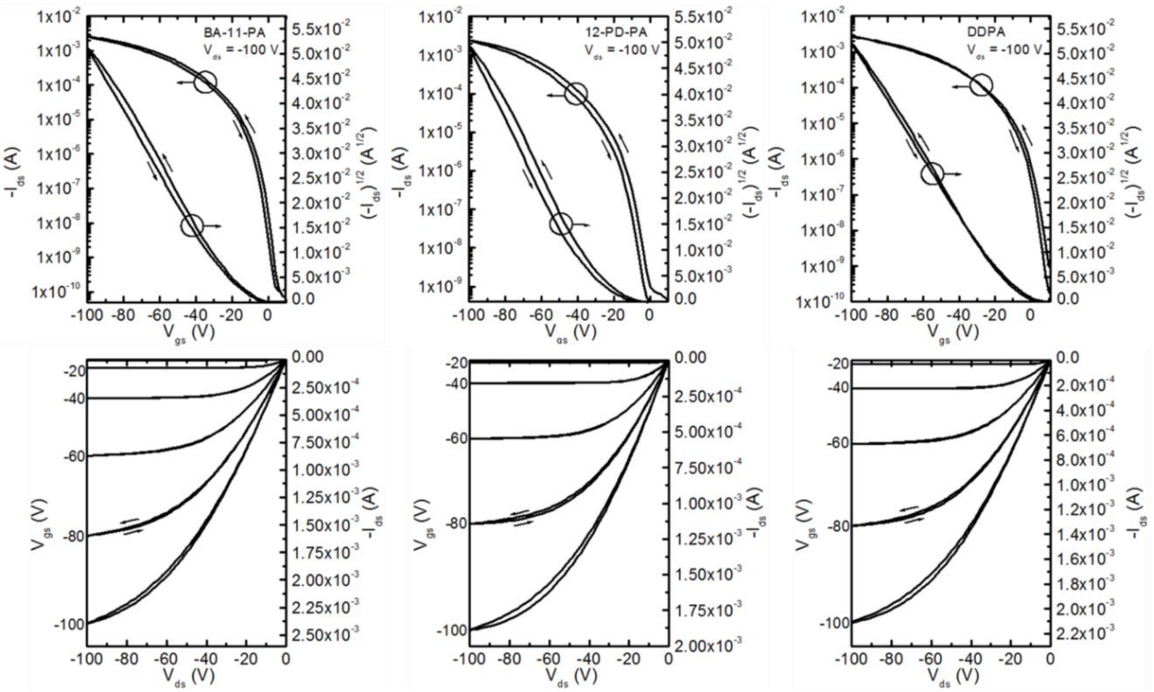

**Figure 6.** Representative transfer and output curves for pentacene devices fabricated on BA-11-PA, 12-PD-PA and DDPA SAMs. Channel length 12 µm, channel width 1000 µm.

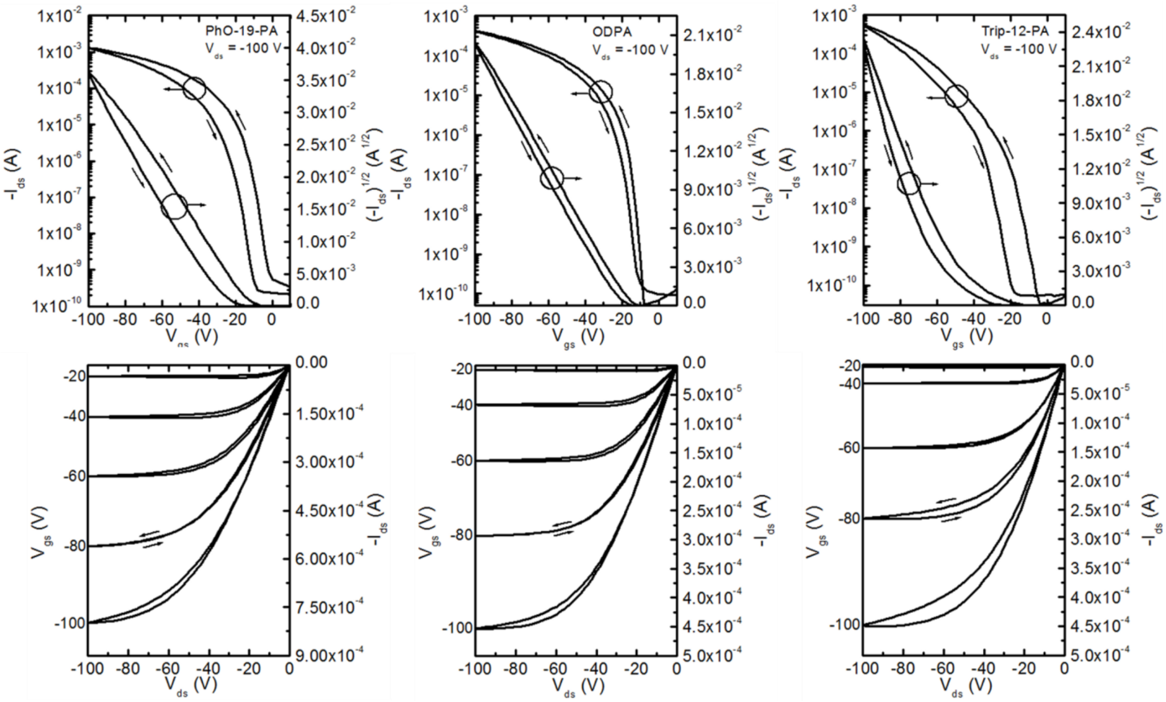

**Figure 7.** Representative transfer and output curves for pentacene devices fabricated on PhO-19-PA, ODPA and Trip-12-PA SAMs. Channel length 12 µm, channel width 1000 µm.

**Table 3.** Summarized pentacene device performance across all SAM platforms. Devices measured had channel length 12 µm and channel width 1000 µm. At least 20 devices were measured on each SAM platform across multiple substrates.

| SAM | $\mu$ ($cm^2 V^{-1} s^{-1}$) (High) Avg. ± Avg. Dev | $V_t$ (V) Avg. ±Avg. Dev. | $S$ (V/Dec) Avg. ± Avg. dev. | $I_{on}/I_{off}$ Highest-Lowest |
|---|---|---|---|---|
| BA-11-PA | (4.0) 3.5 ± 0.28 | 26.0 ± 12.3 | 5.9 ± 2.4 | $3.2 \times 10^7$ - $1.0 \times 10^6$ |
| 12-PD-PA | (3.4) 3.15 ± 0.31 | 14.0 ± 7.3 | 4.3 ± 1.1 | $2.8 \times 10^7$ - $2.2 \times 10^6$ |
| DDPA | (4.1) 3.51 ± 0.39 | 18.6 ± 3.8 | 4.6 ± 2.2 | $5.0 \times 10^7$ - $4.1 \times 10^6$ |
| PhO-19-PA | (0.92) 0.91 ± 0.04 | 22.5 ± 7.5 | 4.0 ± 0.3 | $1.3 \times 10^7$ - $6.9 \times 10^6$ |
| ODPA | (1.3) 0.98 ± 0.21 | 27.4 ± 6.8 | 4.6 ± 2.2 | $1.1 \times 10^7$ - $2.8 \times 10^6$ |
| Trip-12-PA | (0.74) 0.51 ± 0.15 | 42.1 ± 6.7 | 9.2 ± 1.9 | $4.0 \times 10^6$ - $5.0 \times 10^4$ |
| Bare $AlO_x$ | (0.31) 0.23 ± 0.12 | 33.8 ± 9.5 | 16.7 ± 3.2 | $2.5 \times 10^5$ - $4.2 \times 10^4$ |

Pentacene thin film transistors were fabricated by evaporating 50 nm thick Au electrodes onto segregated regions of 40 nm thick pentacene **(Scheme 1)**. Characteristic output and transfer curves for devices on all six SAM surfaces can be found in **Fig. 6** and **Fig. 7,** and summarized device performance specifications for all measured FETs can be found in **Table 3**. From the data presented in **Table 3** it can be clearly seen that substrates coated with BA-11-PA, PD-12-PA and DDPA SAMs exhibit significantly higher device performance than the other SAMs used in this study; at times achieving charge carrier mobilities of $> 4.0$ $cm^2 V^{-1} s^{-1}$. It should be noted that longer SAM molecules of comparable surface energy and structure, exhibit device performance that is inferior. Dielectrics coated with PhO-19-PA, which has comparable surface energy and similar structure to 12-PD-PA, show much smaller pentacene grains and mobility measurements approximately 75% lower. The triptycene-based SAM of Trip-12-PA, which has comparable chain length and surface energy to the BA-11-PA molecule, exhibited the worst device performance of all SAM structures.

When comparing charge mobility values presented here it is important to keep in mind typical values for pentacene FET devices fabricated on an unmodified oxide dielectrics. Measurements of 0.1-0.3 $cm^2\ V^{-1}\ s^{-1}$ are commonly observed in our research group for this surface and are accompanied by large hysteresis and threshold voltage values **(Table 3)**. As shown here, with a properly chosen SAM molecular structure, charge carrier mobility of 15-20 times larger can be achieved in conjunction with low threshold voltage and minimal hysteresis. From these results, two trends can be identified: First, devices in which dielectrics have been coated with SAMs possessing non-bulky terminal groups and alkyl chain of $\sim(CH_2)_{12}$ exhibit much higher pentacene charge carrier mobility in comparison to bulky or long SAMs. Second, surface energy appears to be randomly correlated with pentacene growth and charge carrier mobility.

### *Pentacene Device Performance and SAM Structural Order Relationship*

In the past literature many claims have been made about how SAM molecular structure influences pentacene device performance. In older manuscripts SAMs with a high degree of crystalinity were desired to promote high-quality device performance. As introduced in section 2.4, mid length $\sim(CH_2)_{12}$ alkyl-monolayers (DDPA) exist in a liquid-like disordered state promoting high mobility device performance. In this liquid form, molecules are not aligned in a perfect all-trans conformation, and therefore variations in orientation and meeting of two grains do not affect the SAM surface. It is shown here that this same principal also applies to alkyl-type SAMs modified with different non-bulky terminal groups. The BA-11-PA and 12-PD-PA SAM structures used in this study are shown to be similarly amorphous to DDPA from NEXAFS (**Fig. 4**) and both facilitate the construction of pentacene devices with comparable performance **(Fig.**

**6, Table 3)**. Since the alkyl chains present in these SAM structures are both mid-length-disordered, and the phenyl terminal group is not large enough to promote strong π-π stacking, a disordered surface ideal for pentacene grain growth is formed. This is highly advantageous from a processing standpoint and will be addressed more in the "*Pentacene Device Performance and SAM Surface Energy Relationship*" section.

For PhO-19-PA and ODPA, grain boundaries are present in the crystalline SAM layer promoting small pentacene crystals and reduced charge carrier mobility. When comparing these two structures, pentacene grains are even smaller on the PhO-19-PA SAM which possesses a longer alkyl chain structure.

### *Pentacene Device Performance and SAM Surface Homogeneity Relationship*

A corollary of SAM structure resulting in a smooth surface is the concept of surface homogeneity; defined here as "uninterrupted surface periodicity." In highly ordered (crystalline) SAM structures (PhO-19-PA, ODPA) it can be hypothesized that boundaries between regions of high density SAM, result in molecular scale defects/monolayer grain boundaries. During self-assembly, as sites of monolayer nucleation grow and coalesce, grain boundaries form. Boundaries can best be described as the meeting point of two chemically identical monolayers of different structural orientation and are analogous to classic grains, albeit in two dimensions. These boundaries act as sites of pentacene nucleation, resulting in smaller pentacene grain growth and reduced charge mobility. Mid-length [$\sim(CH_2)_{12}$] simple alkyl-based SAM structures do not allow for these sites of nucleation to exist because their surface structure is liquid-like. As enthalpic gain from van der Waals forces is not sufficient to overwhelm randomization of the

SAM molecules, there is no periodicity to mid-length-SAM surface structure and therefore long-range homogeneity cannot be disrupted.

To test this hypothesis of surface homogeneity, Trip-12-PA was synthesized. The alkyl chain is highly disordered and the SAM is liquid like in nature (**Fig. 4)**, but due to three-dimensional terminal group of triptycene, there will always be molecular-scale dips and peaks in this SAM surface akin to a SAM grain boundary or gauche defects in ordered structures. Accordingly, pentacene grain size is small (**Fig. 5)** and charge mobility measurements are much lower on this platform than all other SAM structures **(Fig. 7, Table 3)**.

### *Pentacene Device Performance and SAM Surface Energy Relationship*

Little correlation is observed between pentacene charge mobility and SAM surface energy. For molecules used in this study, liquid-like SAMs of BA-11-PA, PD-12-PA and DDPA with surface energies ranging from 26.8-55.7 mN $m^{-1}$ have shown similar high performance to one another, and much better performance than highly ordered SAMs of PhO-19-PA and ODPA with different energies **(Table 1, Table 3)**. Although past manuscripts have tried to show a direct causal relationship between surface energy and pentacene device performance, this is not the case here. From the observed experimental results, if a SAM promotes a structurally homogeneous surface, while achieving sufficient density to block all charge traps, the dielectric will provide a high-quality platform for semiconductor nucleation and growth.

Although vacuum deposited pentacene was used in this systematic study for statistical reproducibility, the aforementioned observation is highly impactful in the context of organic device mass production. As surface energy of SAM structures employed to modify dielectric materials approach very low values such as those of DDPA and ODPA SAMs, techniques for solution processing of the semiconducting layer become limited. For instance, spin coating polymers/small molecules on alkyl-SAM surfaces is often not reproducible due to solvent, and subsequently the organic semiconductor de-wet the surface leading to inconstant coverage. This same problem can be observed with dip coating organic semiconductors on hydrophobic substrates. For these kids of solution processing, a mid-level surface energy of SAM with amorphous structural nature is highly desirable (such as BA-11-PA or PD-12-PA).

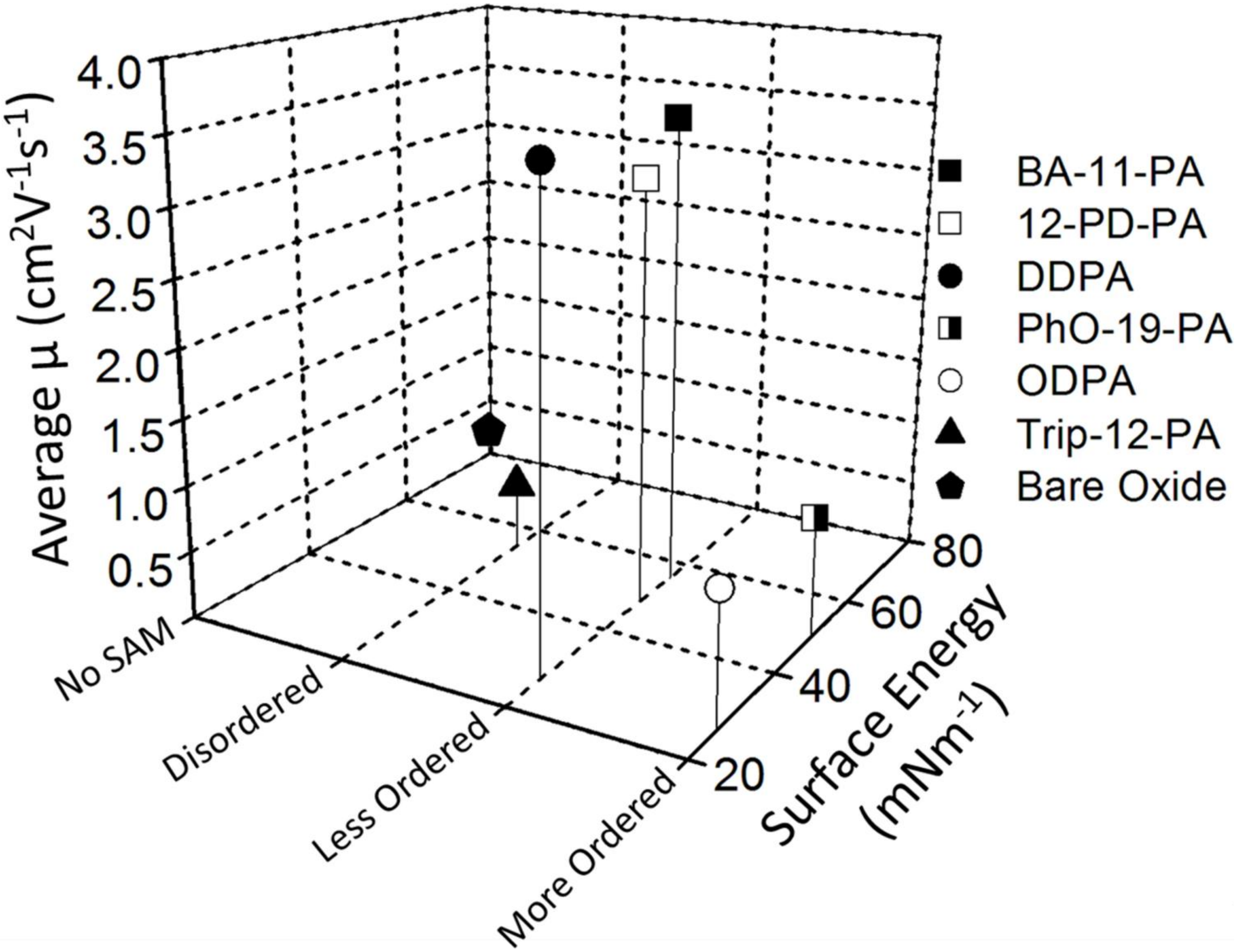

**Scheme 1.** Plot of surface energy (X-axis), SAM alkyl-chain order established by dichroic ratio (Y-axis), and charge carrier mobility of pentacene OFET device (Z-axis) of all six SAM structures and bare $AlO_x/SiO_2$.

*Conclusions*

This study represents a major advancement in understanding the mechanisms at play between SAMs and linear organic semiconducting molecules. A systematic examination of six self-assembled monolayer structures was carried out to better define the relationship between SAM molecular design and pentacene device performance. High charge carrier mobility pentacene OFET devices are demonstrated utilizing self-assembly to promote a favorable pentacene nucleation and growth. Charge carrier mobilities of $> 4.0\ \mathrm{cm}^2\ \mathrm{V}^{-1}\ \mathrm{s}^{-1}$ are observed for less ordered molecular SAM structures with non-bulky methyl-/phenyl- terminal groups and alkyl chains of $\sim(CH_2)_{12}$. The relationship between SAM surface homogeneity and pentacene device performance is probed using NEXAFS, contact angle goniometry and atomic force microscopy. It is concluded that for methyl- and phenyl-terminated SAM structures, pentacene morphology and device performance is primarily dependent on preservation of a homogeneous surface with uninterrupted periodicity. To further validate this conclusion, a triptycene-terminated phosphonic acid molecule with a short alkyl chain was synthesized. Due to the ridged "pronged" nature of the triptycene moiety, surface homogeneity is never preserved regardless of terminal group orientation, and molecular valleys and peaks are formed after dense assembly. Accordingly, pentacene device performance on this SAM surface is greatly impeded.

A variety of SAM structures with a wide range of surface energies were used in this study, and surface energy was examined with respect to pentacene device performance. It was found that surface energy tends to be a negligible factor in device performance provided that the aforementioned conditions for surface homogeneity are met **(Scheme 1)**. This is promising for realizing integration of organic semiconductor devices into mass production, as the mid-level surface energy of phenyl-terminated amorphous SAM structures could potentially provide the platform for reproducible solution processing of high-performance OFETs.

*Experimental*

*Synthesis of PA SAM molecules*

Dodecyl-phosphonic acid (DDPA, **3**) and octadecyl-phosphonic acid (ODPA, **5**) were obtained from PCI Synthesis at 99.9% purity. All other chemicals were purchased from Aldrich or TCI America, and used as received unless otherwise specified. Tetrahydrofuran (THF) was distilled under nitrogen from sodium with benzophenone as the indicator. Methylene chloride was distilled over $P_2O_5$. [8-(11-Phenoxy-undecyloxy)-octyl]-phosphonic acid (PhO-19-PA, **4**) was synthesized following the reported method. $^1$H NMR spectra (300 MHz) were taken on a Bruker-300 FT NMR spectrometer with tetramethylsilane (TMS) as internal reference. Elemental analysis was determined at QTI (Whitehouse, NJ). ESI-MS spectra were obtained on a Bruker Daltonics Esquire Ion Trap Mass Spectrometer.

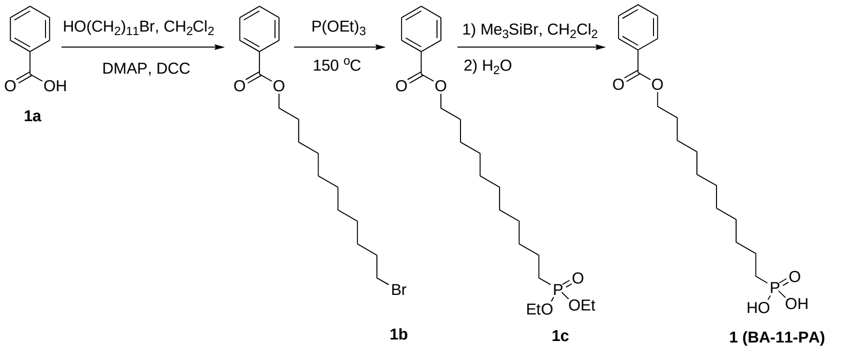

**11-Bromoundecylbenzoate (1b).** To a solution of benzoic acid (0.977 g, 8.0 mmol) and 11-bromoundecanol (2.01 g, 8.0 mmol) in dry methylene chloride (20 mL) under nitrogen was added 4-dimethylaminopyridine (DMAP, 0.293 g, 2.4 mmol) and 1,3-dicyclohexylcarbodiimide (DCC, 2.15 g, 10.4 mmol). The mixture was stirred for 24 h at room temperature. The reaction mixture was filtered and washed with methylene chloride. The collected methylene chloride solution was dried with $Na_2SO_4$, and concentrated. The crude product was purified over silica gel column chromatography with hexane/methylene chloride (1:1) as the eluent to afford a colorless liquid (2.06 g, 73%). $^{1}$H NMR (300 MHz, $CDCl_3$): $\delta$ 8.01-8.07 (m, 2H), 7.40-7.56 (m, 3H), 4.32 (t, 2H, $J$ = 6.9 Hz), 3.40 (t, 2H, $J$ = 6.9 Hz), 1.28-1.88 (m, 18H). $C_{18}H_{27}BrO_2$: Calcd C 60.85, H 7.66, Br 22.49; Found C 60.70, H 7.79, Br 22.57. ESI-MS (*m/z*): Calcd. 354.1; Found 354.1.

**Diethyl 11-(phenylcarboxyl)undecylphosphonate (1c).** A mixture of 1b (1.24 g, 3.5 mmol) and triethyl phosphite (19.10 g, 114.9 mmol, 20.0 mL) was heated under nitrogen at 150 °C for 17 h. The excess of triethyl phosphite was removed by distillation under vacuum. The crude product was purified over silica gel column chromatography with methylene chloride to methylene chloride/ethyl acetate (1:1) as the eluents to afford a colorless liquid (1.27 g, 88%). $^{1}$H NMR (300 MHz, $CDCl_3$): $\delta$ 8.01-8.07 (m, 2H), 7.40-7.56 (m, 3H), 4.31 (t, 2H, $J$ = 6.9 Hz), 4.04-4.14 (m, 4H), 1.28-1.80 (m, 26H). $C_{22}H_{37}O_5P$: Calcd C 64.06, H 9.04, P 7.51; Found C 63.92, H 9.20, P 7.44. ESI-MS (*m/z*): Calcd. 412.2; Found 412.3.

**Benzoic acid 11-phosphono-undecyl ester (BA-11-PA, 1).** To a solution of 1c (0.619 g, 1.5 mmol) in dry methylene chloride (15 mL) under nitrogen was dropwise added bromotrimethylsilane (1.38 g, 1.17 mL, 9.0 mmol). The mixture was stirred for 22 h at room temperature. The reaction mixture was poured into water (200 mL), filtered and washed with large amount of water to collect a white solid (0.517 g, 97%). $^{1}$H NMR (300 MHz, $CDCl_3$): $\delta$ 8.01-8.06 (m, 2H), 7.41-7.56 (m, 3H), 4.30 (t, 2H, $J$ = 6.9 Hz), 1.28-1.82 (m, 20H). $C_{18}H_{29}O_5P$: Calcd C 60.66, H 8.20, P 8.69; Found C 60.51, H 8.32, P 8.54. ESI-MS (*m/z*): Calcd. 356.2; Found 356.1.

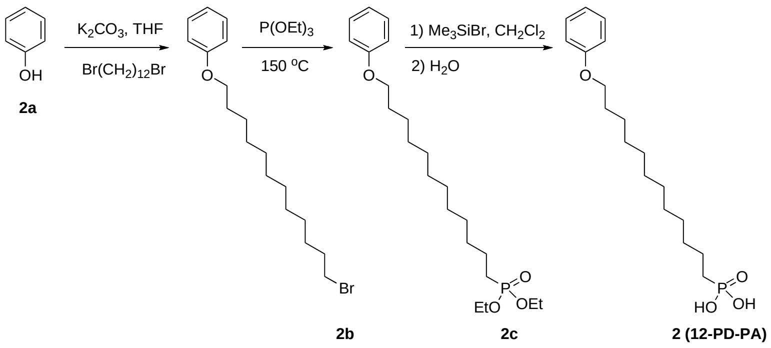

**12-Bromododecoxybenzene (2b).** To a solution of phenol (1.88 g, 20.0 mmol) and 1,12-dibromododecane (6.56 g, 20.0 mmol) in dry THF (50 mL) under nitrogen was added potassium carbonate (4.15 g, 30.0 mmol). The mixture was stirred for 17 h under reflux, cooled down to room temperature and filtered to remove insoluble salts. The filtrate was concentrated by rotary evaporation under reduced pressure. The crude product was purified over silica gel column chromatography with hexane/methylene chloride (3:1) as the eluent to afford a white solid (4.17 g, 61%). $^1$H NMR (300 MHz, $CDCl_3$): $\delta$ 7.24-7.31 (m, 2H), 6.87-6.96 (m, 3H), 3.95 (t, 2H, $J$ = 6.6 Hz), 3.41 (t, 2H, $J$ = 6.9 Hz), 1.27-1.89 (m, 20H). $C_{18}H_{29}BrO$: Calcd C 63.34, H 8.56, Br 23.41; Found C 63.19, H 8.65, Br 23.33. ESI-MS (*m/z*): Calcd. 340.1; Found 340.2.

**Diethyl 12-phenoxydodecylphosphonate (2c).** A mixture of 2b (1.28 g, 3.75 mmol) and triethyl phosphite (19.10 g, 114.9 mmol, 20.0 mL) was heated under nitrogen at 150 $^o$C for 18 h. The excess of triethyl phosphite was removed by distillation under vacuum. The crude product was purified over silica gel column chromatography with methylene chloride to methylene chloride/ethyl acetate (1:1) as the eluents to afford a white solid (1.26 g, 85%). $^1$H NMR (300 MHz, $CDCl_3$): $\delta$ 7.24-7.31 (m, 2H), 6.87-6.96 (m, 3H), 4.02-4.15 (m, 4H), 3.95 (t, 2H, $J$ = 6.6 Hz), 1.26-1.81 (m, 28H). $C_{22}H_{39}O_4P$: Calcd C 66.30, H 9.86, P 7.77; Found C 66.15, H 9.97, P 7.69. ESI-MS (*m/z*): Calcd. 398.3; Found 398.3.

**(12-Phenoxy-dodecyl)-phosphonic acid (12-PD-PA, 2).** To a solution of 2c (0.598 g, 1.5 mmol) in dry methylene chloride (15 mL) under nitrogen was dropwise added bromotrimethylsilane (1.38 g, 1.17 mL, 9.0 mmol). The mixture was stirred for 19 h at room temperature. The reaction mixture was poured into water (200 mL), filtered and washed with large amount of water to collect a white solid (0.472 g, 92%). $^1$H NMR (300 MHz, $CDCl_3$): $\delta$ 7.24-7.31 (m, 2H), 6.87-6.96 (m, 3H), 3.95 (t, 2H, $J$ = 6.6 Hz), 1.27-1.81 (m, 22H).$C_{18}H_{31}O_4P$: Calcd C 63.14, H 9.13, P 9.05; Found C 62.96, H 9.24, P 8.97. ESI-MS (*m/z*): Calcd. 342.2; Found 342.2.

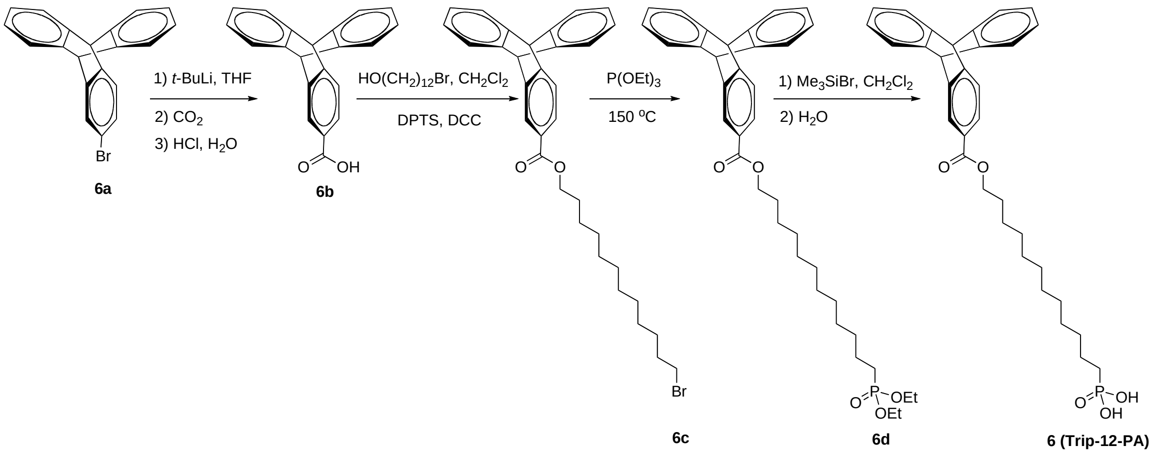

**2-Triptycenylcarboxylic acid (6b).** 2-Bromotriptycene (1.00 g, 3.0 mmol) was added to a dry THF (10 mL) and cooled to -78 °C in a dry ice/acetone bath for 20 min. *Tert*-butyllithium (3.53 mL, 1.7 M in THF, 6.0 mmol) was added dropwise and the mixture was cooled for another 20 min. The mixture was then warmed up to 0 °C for 20 min and then re-cooled to -78 °C. After 20 min, $CO_2$ (dry ice) was crushed and placed in a closed flask. The carbon dioxide gas was transferred via needle and bubbled into the solution at -78 °C for 30 min. After bubbling, the cloudy mixture was acidified with 2M HCl until the solution was acidic. The solution was removed, washed with water, extracted with ethyl acetate, and dried over sodium sulfate. Following evaporation in vacuo, the residue was purified over silica gel column chromatography with hexanes/ethyl acetate (10:1 to 6:1) as the eluents to afford a faint yellowish white solid (0.610 g, 68%). $^1$H NMR (500 MHz, DMSO-$d_6$): $\delta$ 12.81 (broad s, 1H), 8.00 (s, 1H), 7.65 (d, 1H, *J* = 7.5 Hz), 7.55 (d, 1H, *J* = 7.5 Hz), 7.45 (m, 4H), 7.01 (m, 4H), 5.78 (s, 1H), 5.75 (s, 1H). $^{13}$C NMR (125 MHz, $CDCl_3$): $\delta$ 27.1, 53.9, 54.1, 54.2, 123.7, 123.9, 125.1, 125.2, 125.5, 125.6, 126.2, 128.3, 144.2, 144.7, 145.3, 145.9, 151.5, 172.2. $C_{21}H_{14}O_2$: Calcd C 84.54, H 4.73; Found C 84.41, H 4.84. ESI-MS (*m/z*): Calcd. 298.1; Found 297.3.

**1-(2-Triptycenylcarboxy)-12-bromododecane (6c).** To a solution of 6b (0.312 g, 1.05 mmol) and 12-bromododecanol (0.308 g, 1.16 mmol) in dry methylene chloride (20 mL) under nitrogen was added 4-(dimethylamino)pyridium 4-toluenesulfonate (DPTS, 88.3 mg, 0.30 mmol) and 1,3-dicyclohexylcarbodiimide (DCC, 0.402 g, 1.95 mmol). The mixture was stirred for 24 h at room temperature. The reaction mixture was filtered and washed with methylene chloride. The collected methylene chloride solution was dried with $Na_2SO_4$, and concentrated. The crude product was purified over silica gel column chromatography with hexane/methylene chloride (3:1 to 1:1) as the eluents to afford a slightly yellow viscous liquid (0.309 g, 54%). $^1$H NMR (300 MHz, $CDCl_3$): $\delta$ 8.04 (s, 1H), 7.73 (d, 1H, *J* = 7.5 Hz), 7.39-7.46 (m, 5H), 6.98-7.03 (m, 4H), 5.51 (s, 1H), 5.49 (s, 1H), 4.25 (t, 2H, *J* = 6.6 Hz), 3.41 (t, 2H, *J* = 6.6 Hz), 1.22-1.95 (m, 20H). $C_{33}H_{37}BrO_2$: Calcd C 72.65, H 6.84, Br 14.65; Found C 72.50, H 6.97, Br 14.59. ESI-MS (*m/z*): Calcd. 544.2; Found 544.1.

**Diethyl 12-(2-triptycenylcarboxy)dodecylphosphonate (6d).** A mixture of 6c (0.302 g, 0.55 mmol) and triethyl phosphite (9.55 g, 53.5 mmol, 10.0 mL) was heated under nitrogen at 150 °C for 18 h. The excess of triethyl phosphite was removed by distillation under vacuum. The crude product was purified over silica gel column chromatography with methylene chloride to methylene chloride/ethyl acetate (1:1) as the eluents to afford a white solid (0.189 g, 57%). $^1$H NMR (300 MHz, $CDCl_3$): $\delta$ 8.04 (s, 1H), 7.73 (d, 1H, *J* = 7.5 Hz), 7.38-7.46 (m, 5H), 6.98-7.03 (m, 4H), 5.51 (s, 1H), 5.49 (s, 1H), 4.25 (t, 2H, *J* = 6.6 Hz), 4.05-4.15 (m, 4H), 1.24-1.96 (m, 28H). $C_{37}H_{47}O_5P$: Calcd C 73.73, H 7.86, P 5.14; Found C 73.61, H 7.97, P 5.07. ESI-MS (*m/z*): Calcd. 602.3; Found 602.2.

**12-(2-Triptycenylcarboxy)dodecylphosphonic acid (Trip-12-PA, 6).** To a solution of 6d (0.183 g, 0.30 mmol) in dry methylene chloride (15 mL) under nitrogen was dropwise added bromotrimethylsilane (0.276 g, 0.23 mL, 1.80 mmol). The mixture was stirred for 28 h at room temperature. The reaction mixture was poured into water (200 mL), filtered and washed with large amount of water to collect a white solid (0.151 g, 92%). $^1H$ NMR (300 MHz, $CDCl_3$): $\delta$ 8.04 (s, 1H), 7.73 (d, 1H, *J* = 7.5 Hz), 7.37-7.46 (m, 5H), 6.97-7.04 (m, 4H), 5.51 (s, 1H), 5.49 (s, 1H), 4.26 (t, 2H, *J* = 6.6 Hz), 1.25-1.98 (m, 22H). $C_{33}H_{39}O_5P$: Calcd C 72.51, H 7.19, P 5.67; Found C 72.37, H 7.30, P 5.58. ESI-MS (*m/z*): Calcd. 546.3; Found 546.3.

### *Substrate Preparation and $AlO_x$ Formation*

Heavily P-doped silicon substrates with 300 nm thermally grown oxide were cleaned by piranha etching $H_2SO_4$:$H_2O_2$ (3:1 by volume) for 10 minutes, followed by immersion in $H_2O$:$H_2O_2$:$NH_4OH$ (5:1:1 by volume) and through rinsing in DI $H_2O$. Clean substrates were placed in a Diener Femto low-pressure air plasma system for 10 minutes beneath an overhanging aluminum electrode operating at 40 kHz. This has been shown by our group to deposit a ~2.5 nm thick layer of $AlO_x$ on substrate surfaces as previously verified by time of flight secondary ion mass spectroscopy (TOF-SIMS).

### *Self-Assembly and SAM cleaning*

All self-assembly was carried out overnight (16 hrs) in 0.1 mM solutions at ambient conditions. For BA-11-PA, 12-PD-PA, PhO-19-PA, DDPA, and ODPA, tetrahydrofuran (THF) was used as solvent. For Trip-12-PA, chloroform was used as solvent.

Once substrates were removed from their respective assembly solutions, residual compound was removed by 10-min sonication in baths of clean solvent. BA-11-PA coated substrates were cleaned by sonication in 1:20 triethylammine (TEA):THF followed by THF and ethanol (EtOH). 12-PD-PA and PhO-19-PA were cleaned by sonication in 1:20 TEA:Dimethylfommamide (DMF), followed by THF and EtOH. DDPA and ODPA were cleaned by sonication in THF then hexanes. Trip-12-PA was cleaned by sonication in 1:20 TEA:chloroform, followed by chloroform and EtOH.

### *SAM Surface Characterization (AFM)*

To ensure residual compound had been successfully removed from the substrate surface, SAMs were examined with atomic force microscopy (AFM). Images were taken in tapping mode using a Miltimode Nanoscope III atomic force microsope made by Digital Instruments. Etched silicon tips were used with resonant frequencies between 300 and 350 kHz. Roughness measurements were calculated using NanoScope Analysis V1.20. Images of pentacene grain morphology were also aquired in this way.

### *Surface Energy Measurments and Calculations*

Surface energy was measured by contact angle goniometry utilizing the well-established Wu (harmonic mean) method. Diiodomethane (DIM) and deionized water were used as probe solvents. The contact angles of five droplets of DI $H_2O$ and diiodomethane were averaged to calculate dispersion and polar components. All measurements were in very good agreement with one another as no more than 3° in contact angle deviation was seen between any two measurements on the same SAM surface.

### *SAM Characterization (NEXAFS)*

NEXAFS spectra were collected at the National Synchrotron Light Source (NSLS) U7A beamline at Brookhaven National Laboratory, which uses an elliptically polarized beam with about 85% p-polarization. For the experiments we used a monochromator with a 600 l/mm grating that provides a full-width at half-maximum (FWHM) resolution of ~0.15 eV at the carbon K-edge (285 eV). The monochromator energy scale was calibrated using the 285.35 eV C 1s – π*(C=C) transition on a graphite transmission grid placed in the path of the X-rays. To suppress artifacts by incident beam intensity variation and monochromator absorption features, the spectra were normalized by the spectrum of an upstream gold-coated mesh prepared by evaporation of gold in vacuo. Both the reference and signal were divided by the beam flux as a function of the photon energy prior to normalization. Partial electron yield was monitored by a detector with the threshold voltage maintained at -150 V. Samples were mounted to allow rotation about the vertical axis to change the angle between the sample surface and the incident X-ray beam. The NEXAFS angle is defined as the angle between the incident X-ray beam and the sample surface.

*Pentacene Device Fabrication and Characterization*

Although self-assembly and SAM cleaning was performend in ambient conditions, once complete, substrates were placed in a dry $N_2$ golvebox environment containing thermal evaporator (Angstom Engineering)/probe station and never again exposed to air. Segregated regions of pentacene were thermally evaporated onto the various SAM surfaces at a rate of 0.2 Å $s^{-1}$ for a final thickenss of 40 nm and patterned by shadow mask. During evapoaration substrates were heald at a constant temperatre of 60 °C; once complete, substrates were kept at high vaccum and allowed to cool to room temperature overnight. Gold source and drain electrodes were patterned by shadow mask and evaporated at 1 Å $s^{-1}$ for a final thickenss of 50 nm.

Pentacene devices were characterized in a dry $N_2$ environment using an Agilent 4155B semiconductor parameter analyzer. Field effect mobility ($\mu$) was calculated in the saturation regime using a linear fit of $(-I_{ds})^{1/2}$ vs. $V_{gs}$. Threshold voltage ($V_t$) was calculated as the x-intercept of the linear section of the $(I_{ds})^{1/2}$ versus $V_{gs}$ plot. Subthreshold swing ($S$) was calculated by the inverse slope of $I_{ds}$ versus $V_{gs}$ in the region of exponential current increase. All devices measured had channel length of 12 µm and width of 1000 µm. At least 20 devices were measured on each SAM surface spreading over multiple substrates.

## Solid-State Densification of Spun-Cast Self-Assembled Monolayers for Use in Ultra-Thin Hybrid Dielectrics

Ultra-thin self-assembled monolayer (SAM)-oxide hybrid dielectrics have gained significant interest for their application in low-voltage organic field effect transistors (OFETs).[65, 66] In “Solid State Densification of Spun-Cast Self Assembled Monolayers for Use In Ultra-Thin Hybrid Dielectrics,” [8-(11-Phenoxy-undecyloxy)-octyl]phosphonic acid (PhO-19-PA) SAM on ultrathin $AlO_x$ (2.5 nm) was developed to significantly enhance dielectric performance of inorganic oxides through reduction of leakage current while maintaining similar capacitance to the underlying oxide structure. Rapid processing of this SAM in ambient conditions was achieved by spin coating, however, as-cast monolayer density was not sufficient for dielectric applications. Thermal annealing of the bulk spun-cast PhO-19-PA molecular film was explored as a mechanism for densification. SAM density, surface coverage, and order were examined as a function of annealing temperature. These SAM characteristics were probed through atomic force microscopy (AFM), X-ray photoelectron spectroscopy (XPS), and near edge X-ray absorption fine structure spectroscopy (NEXAFS). It was found that at temperatures sufficient to melt the as-cast bulk molecular film, SAM densification is achieved; leading to a rapid processing technique for high performance SAM –oxide hybrid dielectric systems utilizing a single wet processing step. To demonstrate low-voltage devices based on this hybrid dielectric (with leakage current density of $7.7\text{x}10^{-8}$ A/cm$^2$ and capacitance density of 0.62 μF/cm$^2$ at 3 V), pentacene thin-film transistors (OTFTs) were fabricated and yielded sub 2 V operation and charge carrier mobilites of up to 1.1 cm$^2$ V$^{-1}$ s$^{-1}$.

Manipulation of the dielectric layer has been accomplished both through organic and inorganic means, however, recently hybrid inorganic/organic ultra-thin dielectric materials have attracted attention for their robust insulating properties and ease of processing.[56] One method of obtaining these hybrid structures is through merging inorganic oxides and self-assembled monolayers (SAMs).[67] This technique has been demonstrated by several groups and has proven to be quite successful, allowing the formation of sufficiently insulative layers that are less than 10 nm in thickness.[68] Through molecular design, electronic properties of these structures can be tailored to meet the needs of a wide variety of device constraints. However, several obstacles have yet to be overcome in order to make this approach to forming OFET dielectrics ubiquitous.

Dense and ordered PA self-assembly is typically accomplished by lengthy immersion time in dilute solutions, sometimes in excess of 16 hours.[36] Well packed SAM structures have been achieved by rapid spin coating processes. However, dense assembly by spin casting is often only completed with simple alkyl-structures that do not provide steric hindrance sufficient to block other SAM molecules from reaching the substrate surface and binding.[69] In this manuscript, chemically complex aryl-alkyl-PA SAMs are formed by spin coating a molecular multilayer. Through thermal annealing of the bulk film, rather than subsequent wet processes, rapid densification is achieved, conserving solvent, compound, and time. Characterization of this processing technique is examined through various spectroscopic methods and proven to facilitate the spin casting of SAMs with complex molecular structures that exhibit non-negligible steric effects during self-assembly.

## *Materials*

The PhO-19-PA, [8-(11-Phenoxy-undecyloxy)-octyl]phosphonic acid, molecule was synthesized through the following procedures.

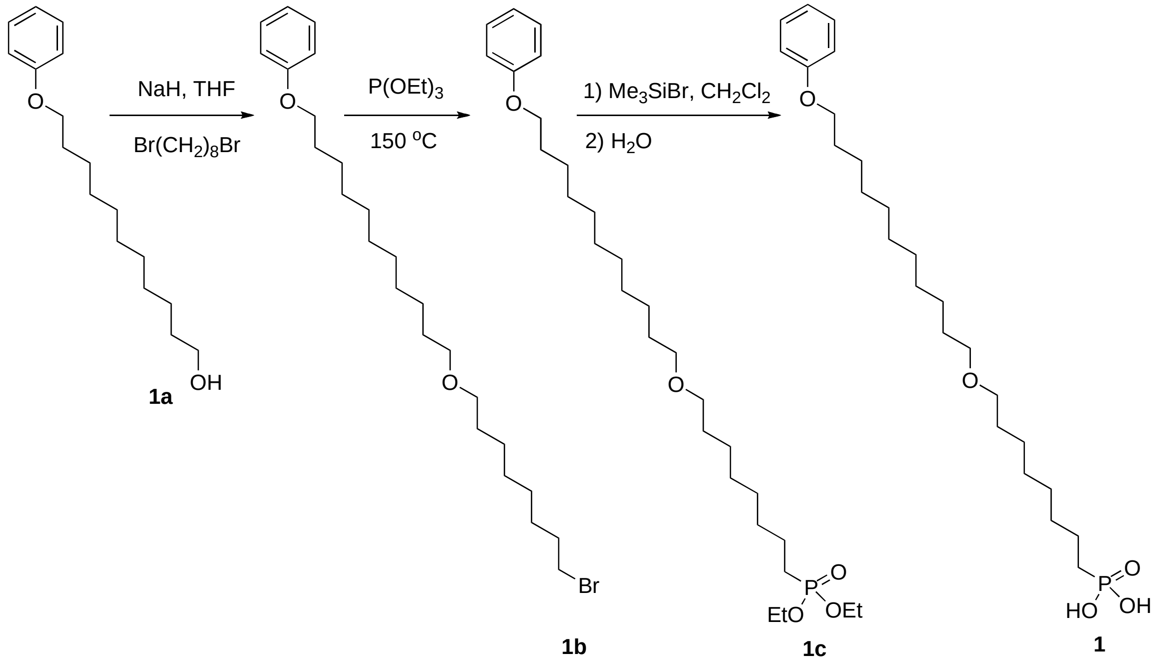

All chemicals were purchased from Aldrich and used as received unless otherwise specified. Tetrahydrofuran (THF) was distilled under nitrogen from sodium with benzophenone as the indicator. Methylene chloride was distilled over $P_2O_5$. 11-Phenoxy-1-undecanol (**1a**) was synthesized following the reported method. $^1$H NMR spectra (300 MHz) were taken on a Bruker-300 FT NMR spectrometer with tetramethylsilane (TMS) as internal reference. Elemental analysis was determined at QTI (Whitehouse, NJ). ESI-MS spectra were obtained on a Bruker Daltonics Esquire Ion Trap Mass Spectrometer.

11-(8-Bromooctoxy)undecoxybenzene (1b). To a mixture of 1,8-dibromooctane (3.26 g, 12.0 mmol) and sodium hydride (0.384 g, 16.0 mmol) in dry THF (30 mL) under nitrogen was dropwise added the solution of 11-phenoxy-1-undecanol (**1a**) (1.06 g, 4.0 mmol) in dry THF (5 mL). The mixture was stirred overnight under reflux, cooled down to room temperature and filtered to remove insoluble salts. The filtrate was concentrated by rotary evaporation under reduced pressure. The crude product was purified over silica gel column chromatography with hexane/methylene chloride (3:1) as the eluent to afford a white solid (1.43 g, 79%). $^1$H NMR (300 MHz, $CDCl_3$): $\delta$ 7.27-7.33 (m, 2H), 6.89-6.98 (m, 3H), 3.97 (t, 2H, $J$ = 6.6 Hz), 3.38-3.45 (m, 6H), 1.25-1.91 (m, 30H). $C_{25}H_{43}BrO_2$: Calcd C 65.92, H 9.51, Br 17.54; Found C 66.07, H 9.58, Br 17.46. ESI-MS (*m/z*): Calcd. 454.2; Found 454.1.

Diethyl 8-(11-phenoxy)undecoxyoctylphosphonate (1c). A mixture of **1b** (0.91 g, 2.0 mmol) and triethyl phosphite (9.55 g, 10.0 mL) was heated under nitrogen at 150 °C for 20 h. The excess of triethyl phosphite was removed by distillation under vacuum. The crude product was purified over silica gel column chromatography with methylene chloride to methylene chloride/ethyl acetate (5:1) as the eluents to afford a white solid (0.72 g, 70%). $^1$H NMR (300 MHz, $CDCl_3$): $\delta$ 7.23-7.31 (m, 2H), 6.87-6.90 (m, 3H), 4.04-4.12 (m, 4H), 3.95 (t, 2H, $J$ = 6.6 Hz), 3.35-3.42 (m, 4H), 1.28-1.81 (m, 38H). $C_{29}H_{53}O_5P$: Calcd C 67.94, H 10.42, P 6.04; Found C 68.05, H 10.51, P 5.95. ESI-MS (*m/z*): Calcd. 512.4; Found 512.4.

8-(11-Phenoxy)undecoxyoctylphosphonic acid (1). To a solution of **1c** (0.385 g, 0.75 mmol) in dry methylene chloride (20 mL) under nitrogen was dropwise added bromotrimethylsilane (0.689 g, 0.58 mL, 4.50 mmol). The mixture was stirred overnight at room temperature. The reaction mixture was poured into water (200 mL), filtered and washed with large amount of water to collect a white solid (0.272 g, 80%). $^1$H NMR (300 MHz, $CDCl_3$): $\delta$ 7.50-7.95 (s, br, 2H), 7.23-7.30 (m, 2H), 6.80-6.95 (m, 3H), 3.95 (t, 2H, $J$ = 6.6 Hz), 3.35-3.42 (m, 4H), 1.10-1.80 (m, 32H). $C_{25}H_{45}O_5P$: Calcd C 65.76, H 9.93, P 6.78; Found C 65.87, H 10.02, P 6.71. ESI-MS (*m/z*): Calcd. 456.3; Found 456.3.

*Substrate Preparation*

Heavily P-doped native oxide silicon substrates were cleaned by piranha etching $H_2SO_4$:$H_2O_2$ (volume ratio, 3:1) for 10 minutes, followed by immersion in $H_2O$:$H_2O_2$:$NH_4OH$ (5:1:1) and through rinsing in DI $H_2O$.

*Dielectric Fabrication*

Clean substrates were placed in a Diener Femto low-pressure air plasma system for 10 minutes directly beneath an overhanging aluminum electrode operating at 40 kHz. This has been shown by our group to deposit a ~2.5nm thick layer of $AlO_x$ on substrate surfaces as previously verified by time of flight secondary ion mass spectroscopy (TOF-SIMS). The PhO-19-PA SAM was prepared on the Si native oxide/$AlO_x$ layer via spin coating from a 3 mM solution in chloroform: tetrahydrofuran (THF) (4:1) at 3k RPM for 30 seconds. The bulk SAM coated substrate was then subject to the appropriate annealing/cleaning conditions used to explore mechanisms of SAM formation. The condition deemed ideal for the assembly of a well ordered SAM with excellent dielectric properties is as follows: post spin coating, the multilayer-covered substrates were subjected to annealing at 140°C for 10 minutes followed by the rinse-off of bulk molecular aggregate. This rinsing process consisted of sonication in triethylamine: dimethylformamide (1:20) for 10 minutes followed by five-minute sonication in THF and five-minute sonication in ethanol. Annealing temperatures above 140 °C were explored, however, no further SAM densification was observed and substrate surface morphology worsened, therefore, these experiments will not be discussed in further detail.

*SAM Characterization*

*Atomic Force Microscopy*

Images were taken in tapping mode using a Miltimode Nanoscope III atomic force microsope made by Digital Instruments. Etched silicon tips were used with resonant frequencies between 300 and 350 kHz. Roughness measurements were calculated using NanoScope Analysis V1.20.

### *Near-Edge X-ray Absorption Fine Structure Spectroscopy (NEXAFS)*

Spectra were measured at the National Synchrotron Light Source (NSLS) U7A beamline at Brookhaven National Laboratory, using an elliptically polarised beam with ~85% *p*-polarisation. A monochromator with 600 l/mm grating provided a full-width at half-maximum (FWHM) resolution of ~0.15 eV at the carbon *K*-edge (285 eV). The monochromator was calibrated using the 285.35 eV C 1s $\pi$-$\pi^*$ transition on a graphite transmission grid placed in the upstream path of the X-rays. Both reference and signal were divided by the NEXAFS signal of a gold-coated reference mesh to account for beam intensity variations.

### *X-Ray Photoelectron Spectroscopy (XPS)*

The SAMs were characterized by XPS with a Kratos AXIS Ultra DLD instrument (Kratos, Manchester, England) in the hybrid mode using a monochromatic $Al_{K\alpha}$ X-ray source (photon energy = 1486.6 eV) and normal emission geometry. The XPS determined compositions were an average from three spots on two replicates. Atomic compositions were calculated from peak areas obtained from 0 - 1100 eV survey scans (C 1s, Au 4f) and selected region scans (O 1s, P 2s, Si 2p) acquired at an analyzer pass energy of 80 eV. A linear background was subtracted for all peak quantifications. The peak areas were normalized by the manufacturer-supplied sensitivity factors and surface concentrations were calculated using Casa XPS software.

### *Dielectric Characterization*

Agilent 4284B LCR Meter was used for dielectric capacitance characterization. Thermally evaporated gold squares (area: $4x10^{-4}$ $cm^2$, evaporated at 1Å/s, 50 nm final thickness) were used as the top electrodes and the electrically conductive heavily P-doped Si substrate was used as a universal bottom electrode.

### *OFET Device Construction*

Substrates with hybrid dielectrics fabricated in the aforementioned manner (see Dielectric Fabrication) were placed in a thermal evaporator and allowed to heat to 60 °C under high vacuum. Pentacene (99.95% Aldrich) was evaporated at 0.2 Å/s until the desired thickness of 40 nm was reached. Substrates were cooled to room temperature under high vacuum prior to the thermal evaporation of source and drain electrodes. Gold electrodes were patterned by shadow mask and evaporated at 1 Å/s for a final thickness of 50 nm.

### *OFET Device Characterization*

Transistor characterization was performed in a dry $N_2$ environment using Agilent 4155B semiconductor parameter analyzer. Field effect mobility ($\mu$) was calculated in the saturation regime using a linear fit of $(-I_{ds})^{1/2}$ vs. $V_{gs}$. Threshold voltage ($V_t$) was calculated as the x-intercept of the linear section of the $(I_{ds})^{1/2}$ versus $V_{gs}$ plot. Subthreshold swing ($S$) was calculated by the inverse slope of $I_{ds}$ versus $V_{gs}$ in the region of exponential current increase.

### *Rationale of Molecular Design*

The PhO-19-PA molecule (**Fig. 8A**) was designed as phenyl-terminated alkylphosphonic acid. It has been demonstrated that aliphatic chain length can substantially influence the ability of molecules to self-assemble in a manner favorable to the enhancement of dielectric properties. Longer chain lengths reduce leakage current and provide a greater barrier for electron tunneling.[70] Conversely, short chain lengths do not provide enough enthalpic gain due to Van der Waals interactions to provide significant ordering effects. Phosphonic acid bound alkyl-chain lengths of 18 $CH_2$ or longer form highly ordered structures, thus PhO-19-PA was specifically designed to maximize this interaction. Aromatic terminal structures are known to improve dielectric properties of SAMs by enhancing intermolecular interaction through π-π stacking.[36] Through integration of the aforementioned molecular design principals, PhO-19-PA molecule attempts to maximize dielectric properties of its SAM while maintaining solubility in a wide range of solvents, making it compatible with the fabrication of many device architectures.

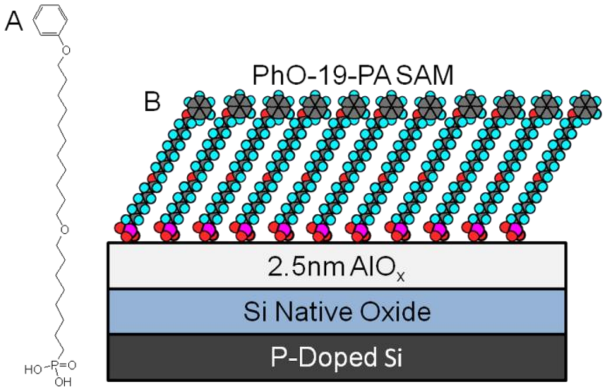

**Figure 8.** (A) Chemical structure of PhO-19-PA molecule. (B) Schematic of hybrid SAM-oxide dielectric used to study SAM densification through solid state annealing.

*Oxide Structure and SAM Formation by Spin Coating.*

The oxide structure used in this study was made by a plasma-enhanced deposition of $AlO_x$ onto the silicon native oxide surface of a highly P-doped wafer. From AFM images it can be seen that this surface has an almost identical morphological appearance to Si native oxide, with an RMS roughness of ~0.2 nm. Following $AlO_x$ deposition, a 3 mM solution of PhO-19-PA is prepared in THF:chloroform (1:4 ) and spun cast onto the substrate at 3k RPM in order to form the remainder of the hybrid dielectric structure (**Fig. 8B**).

Spin coating of phosphonic acid monolayers has been previously investigated by H.-Y. Nie et al. In their work, octadecylphosphonic acid (ODPA) was spun coat onto mica and other oxide surfaces from a 2 mM solution of nonpolar trichloroethane solvent.[69] Post spin coating, substrates were examined under AFM and the portion of the surface covered by ODPA was determined by the ~2 nm variations in height seen between SAM and substrate. From this experiment it was determined that the first spin coating step from a relatively nonpolar solvent results in segregated island-like formations of ODPA on the surface of the substrate. However, subsequent spin coating experiments using more polar solvents resulted in much less dense SAM coverage. It was hypothesized that due to the polar nature of the phosphonic acid binding group and nonpolar nature of the aliphatic chain, organization of ODPA was occurring in solution. In nonpolar solvent, ODPA head groups are pushed towards the air-solvent interface while the tails remain solubilized, forming ordered rafts of phosphonic acid on the surface of the solvent. Upon spin casting, these organized molecular structures are transferred to the substrate when rafts of phosphonic acid head groups come in contact with the oxide surface.

Nie's hypothesis directly pertains to the PhO-19-PA SAM system and forms the basis for the initial SAM assembly step employed here. Islands of highly ordered SAM bound to the $AlO_x$ layer are formed on the substrate surface. Despite this, we believe significant defects are present in the SAM including regions of low density, voids, and molecular-misorientation (**Fig. 9**, **step 1**). As strong Van der Waals forces and π-π interactions are present between PhO-19-PA molecules, a bulk multilayer is present on the surface of the substrate post spin coating. The presence of this multilayer prevents direct examination of bound monolayer by AFM. To examine the underlying SAM a thorough rinsing process in DMF:TEA (20:1), THF, and ethanol was employed. However, after cleaning, it is evident that initial spin coating has indeed resulted in island SAM formation. Post rinsing, boundaries between regions of formed monolayer are clearly present and characterized by dark surface discontinuities in AFM images (**Fig 10-1A**).

After spin casting of the multilayer and rinsing, dielectric properties are less than ideal despite the formation of monolayer islands. Although Nie *et. al.* found that densification of the SAM could be achieved through subsequent spin coating steps, this technique requires additional SAM compound, solvent, and time. As a means of reducing the impact of processing conditions, our group investigated the possibility of using the residual bulk PhO-19-PA on the surface of substrate as the source of compound for additional SAM densification. Through the employment of proper annealing methods it was found that molecular multilayers could be used to sufficiently densify the SAM, resulting in a high quality ultra-thin dielectric, compatible with ambient solution processed device architectures and a single wet processing step. A cartoon representation of proposed mechanisms responsible for densification can be seen in **Fig 9**.

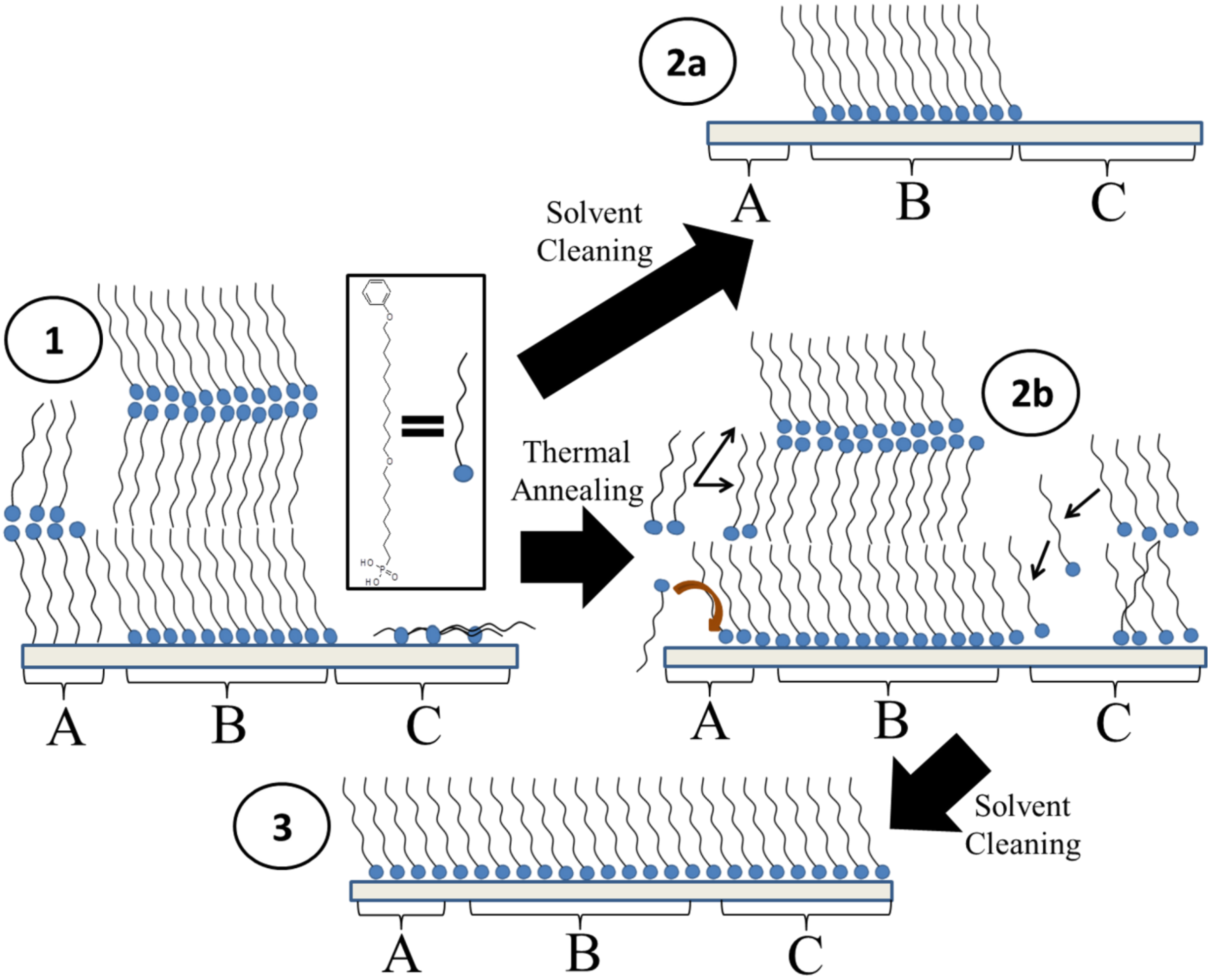

**Figure 9.** Illustration of proposed SAM densification mechanisms. Step 1: Spin coating of disordered as-cast multilayer film. A) PhO-19-PA molecules misoriented and unable to bind with surface. B) Multilayer formation with bound monolayer below. C) SAM lying flat on surface/voids in monolayer due to low density assembly. Step 2a: Multilayer removal prior to annealing, resulting in SAM island formation on substrate surface. A-C) Unbound/misoriented molecules are removed, with bound SAM islands remaining on the surface. Step 2b: Annealing of PhO-19-PA multilayer allowing SAM densification to occur. A) Reorientation of SAM molecules favorable to surface binding. B) Diffusion of SAM molecules across the substrate surface forming large droplets of residual PhO-19-PA material. C) Diffusion of PhO-19-PA across surface; filling in holes and "pushing up" low density structures.

*AFM Characterization*

From AFM images obtained of both the bulk molecular PhO-19-PA film present after spin coating (**Fig. 10, column B**), and underlying SAM made visible through solvent cleaning

(**Fig. 10**, **column A**), dramatic changes in SAM morphology are seen with increased annealing temperatures. Following spin coating without annealing, a bulk molecular layer is clearly shown on the substrate surface (**Fig. 10-1B**), and upon its removal by solvent cleaning, a low-density SAM characterized by large dark grain boundaries on the AFM image is shown (**Fig. 10-1A**). Changes to the substrate surface morphology can be observed when the bulk film is thermally annealed. By heating for 10 minutes at 60°C, the bulk layer begins to transform from a continuous film into a segregated structure (**Fig. 10-3B**). Additionally, voids in the underlying SAM begin to fill, resulting in a more densely packed monolayer (**Fig. 10-3A**). At 80°C the bulk film has melted, forming large grains of residual material and the underlying SAM lacks viable voids by AFM (**Fig. 10-4A & 4B**). For both 100°C and 120°C bulk material left on the surface has formed liquid-like droplets (**Fig. 3-5B & 6B**) and the SAM has the same appearance/similar roughness as bare Si (**Fig. 10-5A & 6A**) (0.2 nm RMS roughness), indicative of a densely packed monolayer. Although further densification occurs up to 140°C, as shown by XPS and NEXAFS, AFM images of the SAM and bulk film at 140°C look identical to those annealed at 120°C and therefore are not shown in **Fig. 3**.

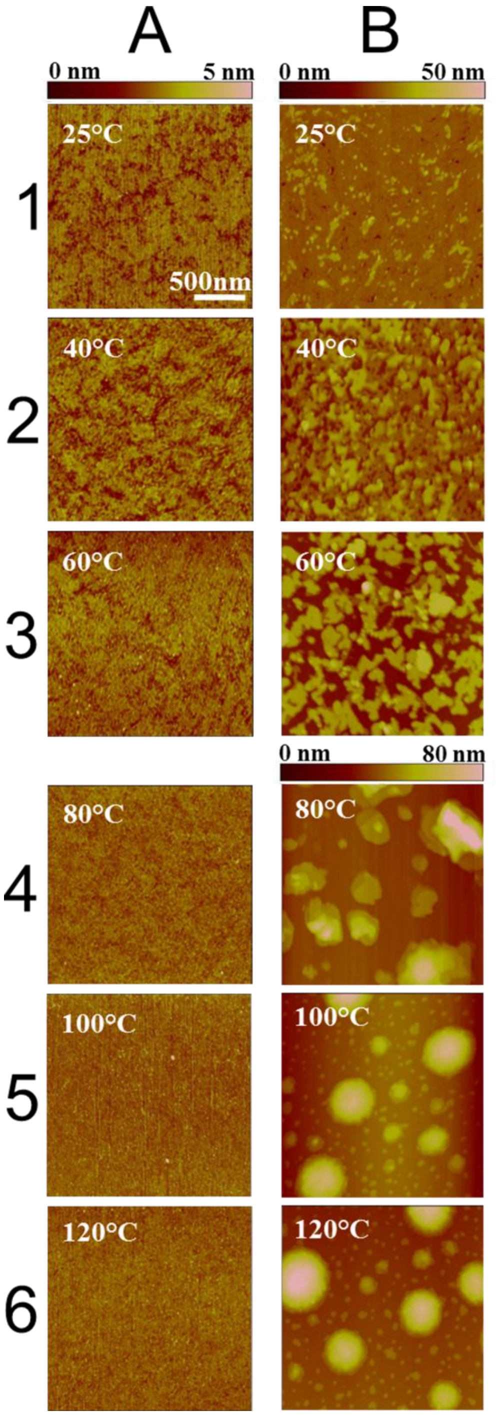

**Figure 10.** PhO-19-PA SAM densification through thermal annealing. (A) AFM images of SAM surface after thermal annealing and solvent cleaning to remove bulk PhO-19-PA multilayer. (B) AFM images of as-cast PhO-19-PA multilayer film after annealing step.

Based on the morphological transitions of the bulk PhO-19-PA molecular film seen at elevated temperature, we propose that SAM densification is occurring by liquefaction of the bulk compound facilitating molecular rearrangement (**Fig. 9**). Upon melting, molecules that did not penetrate into grain boundaries in the SAM during the initial spin coating step are allowed to reorient themselves favorable to surface binding. Through their increased molecular surface mobility due to thermal activation, surface spaces not previously occupied are filled.

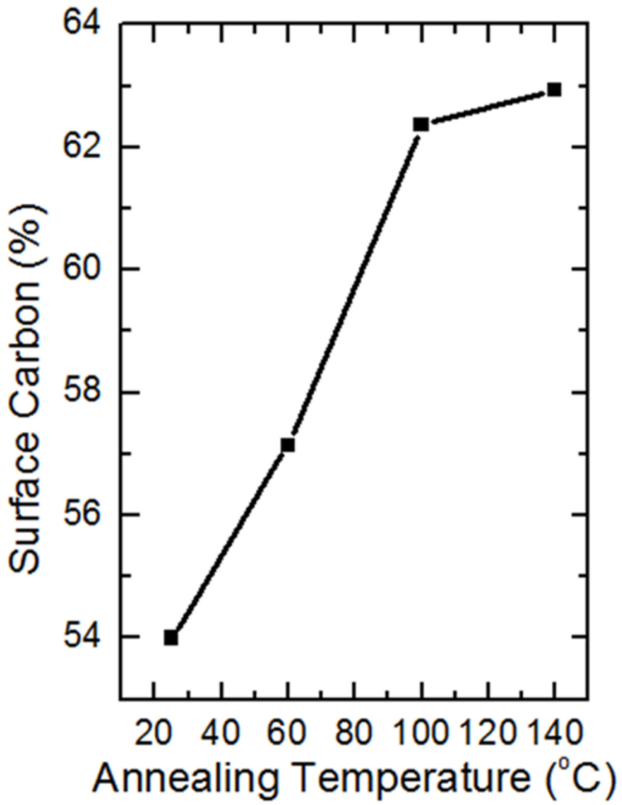

**Figure 11.** Percent carbon in XPS spectra of hybrid SAM-oxide dielectric structure after spun cast bulk film is annealed at 25°C, 60°C, 100°C, and 140°C for 10 min, followed by solvent cleaning, respectively.

*XPS and NEXAFS Analysis*

AFM observations are corroborated with X-ray photoelectron spectroscopy (XPS). Hybrid SAM-oxide dielectric structures after spinning cast bulk film followed by annealing at 25°C, 60°C, 100°C, and 140°C for 10 min, and solvent cleaning, respectively were examined by XPS and showed surface carbon concentration increasing in conjunction with observed densification by AFM (**Fig. 11**). After the initial spin coating process 54% of the first 5 nm of substrate depth is SAM, and by annealing at 140°C, a 9% increase in carbon concentration is achieved. Contrary to AFM images, it is shown that SAM density continues to increase at temperatures well above $T_m$ of the bulk molecular layer up to 140 °C.

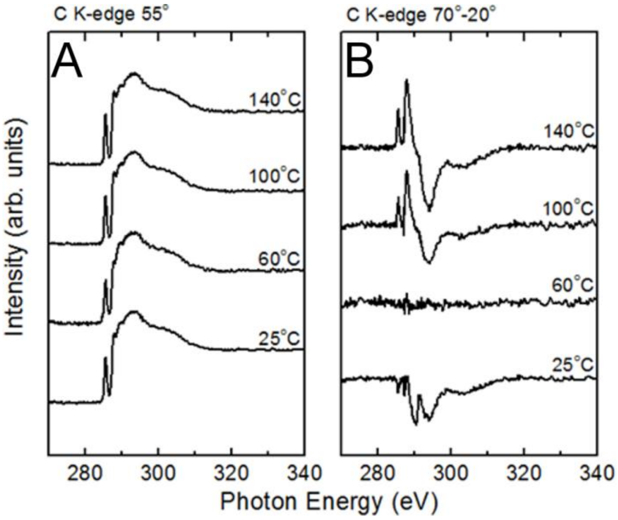

**Figure 12.** NEXAFS spectra of PhO-19-PA SAM after spun cast bulk film is annealed at 25°C, 60°C, 100°C, and 140°C for 10 min., followed by solvent cleaning, respectively. Carbon K-edge 55° (A). Carbon K-edge 70°-20° (B).

The chemical state and structure of the SAMs were also studied with NEXAFS spectroscopy. NEXAFS spectra provided insight into the electronic structure of surfaces by sampling unoccupied molecular orbitals. Structural parameters like alignment, order and orientation in monomolecular films can be probed using the linear dichroism of X-ray absorption by recording the dependence of absorption resonance intensities on the orientation of the electric field vector of the synchrotron X-ray beam with respect to the orientation of molecular orbitals. The linear dichroism can be monitored by measuring spectra at normal and glancing X-ray incidence angles. Spectra collected at 55°, the 'magic angle', are not affected by molecular orientation and are therefore only representative of the electronic and chemical state of the surface.

C *K*-edge spectra for SAMs with different annealing temperatures acquired at an X-ray incidence angle of 55° are presented in **Fig. 12A**. All spectra exhibit an absorption edge related to the excitation of the C 1s electrons into the continuum states and additional characteristic absorption resonances. The spectra show the $\pi_1$* resonance of the terminal phenyl moiety near 285.6 eV. The spectra also exhibit a weak Rydberg resonance (R*) near 287.6 eV mostly related to the aliphatic chains, and broad $\sigma$* resonances related to C-C bonds at higher photon energies. The spectra are very similar and indicate intact SAMs with no indications of C=O or other chemical impurities.

**Fig. 5B** displays the respective 70° - 20° difference spectra. The sample prepared at 25°C shows only a weak dichroism for the $R^*$ resonance, a clear signature of strongly inclined and mostly disordered chains. A difference peak for the phenyl moiety is not detected, indicating the phenyl groups are disordered. The 60°C sample shows no dichroism and the film is most likely mostly disordered. The SAMs annealed at 100°C and 140°C, however, show pronounced linear dichroisms for both the chains and the phenyl groups. The polarity of the difference peaks indicates the phenyl group and the chain are oriented upright. The film annealed with 140°C shows the highest degree of order. We performed a more quantitative analysis of the molecular orientation using relative resonance intensities for the $\pi_1$* and the R$^*$ resonances based on published procedures. The analysis yields tilt angles of 31°±5° and 30°±5° versus the surface normal for the alkyl chains and the phenyl rings, respectively. Similar values have also been observed for well-ordered aliphatic SAMs on gold and $SiO_2$, while thiol SAMs on silver (≈14°), platinum (<15°) and gallium arsenide (≈18°) have shown more upright orientations.[71, 72]

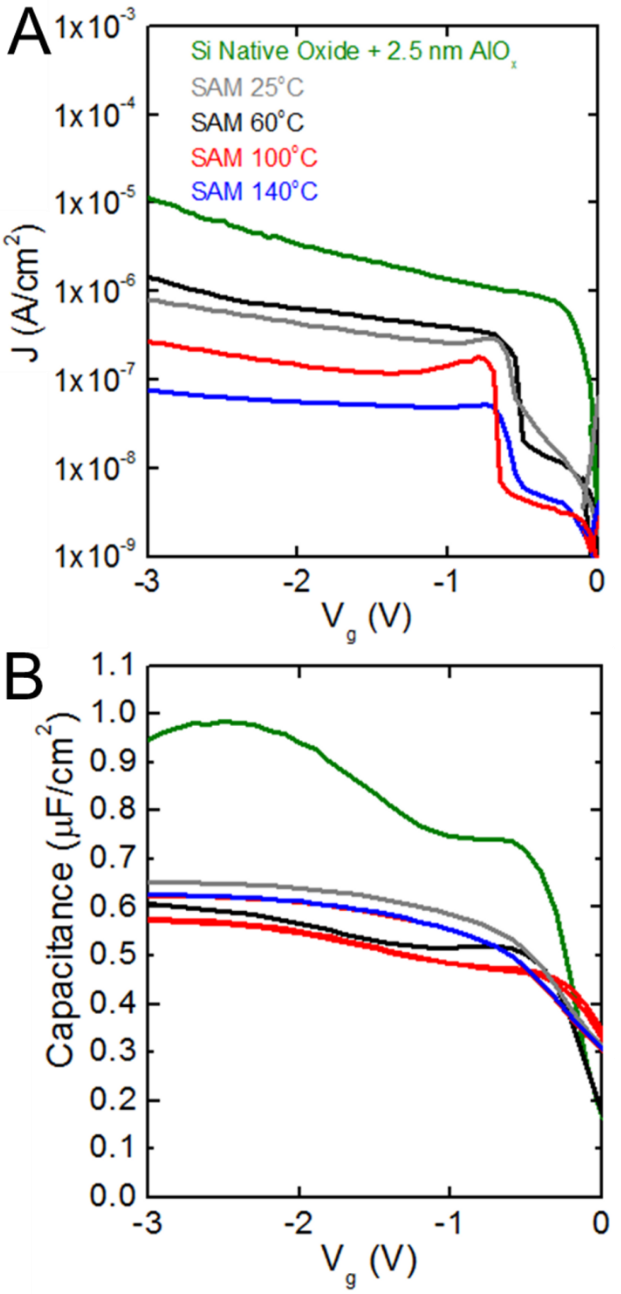

**Figure 13.** Plots of leakage current vs. voltage (A), and capacitance vs. voltage (B) for metal-insulator-semiconductor (MIS) capacitor. Semiconductor: heavily doped P-type Si. Dielectric: SAM on 2.5 nm $AlO_x$ and Si native oxide layers. Metal: 50 nm thermally evaporated Au. Bulk spun cast PhO-19-PA films were annealed at temperatures of 25°C, 60°C, 100°C, 140°C for 10 min, followed by solvent cleaning, respectively, to result in SAMs of increasing density and dielectric performance.

*Dielectric Characterization*

To further evaluate the mechanism of densification and examine the effectiveness of the PhO-19-PA SAM-oxide structure as a dielectric, leakage current and breakdown voltage were evaluated (**Fig. 13**). To quantify the effect of the SAM, dielectric properties of the $AlO_x$/Si native oxide layer were first analyzed resulting in very high leakage currents ($10^{-5}$ A/cm$^2$) at three volts, and low breakdown voltages (~ 4V), making it unsuitable for a dielectric material. Upon initial application of the SAM, a several order of magnitude drop in 3-volt-leakage-current can be observed. After annealing the bulk film, large drops in leakage current are demonstrated. Most notably, at 140 °C, leakage current reaches $7.7 \times 10^{-8}$ A/cm$^2$. Although reduction of leakage current several orders in magnitude is facilitated by the addition of the SAM to the underlying $AlO_x$/Si native oxide layer, capacitance with respect to applied voltage changes little with the presence of the monolayer, dropping from 0.96 µF/cm$^2$ to 0.62 µF/cm$^2$ at three volts.

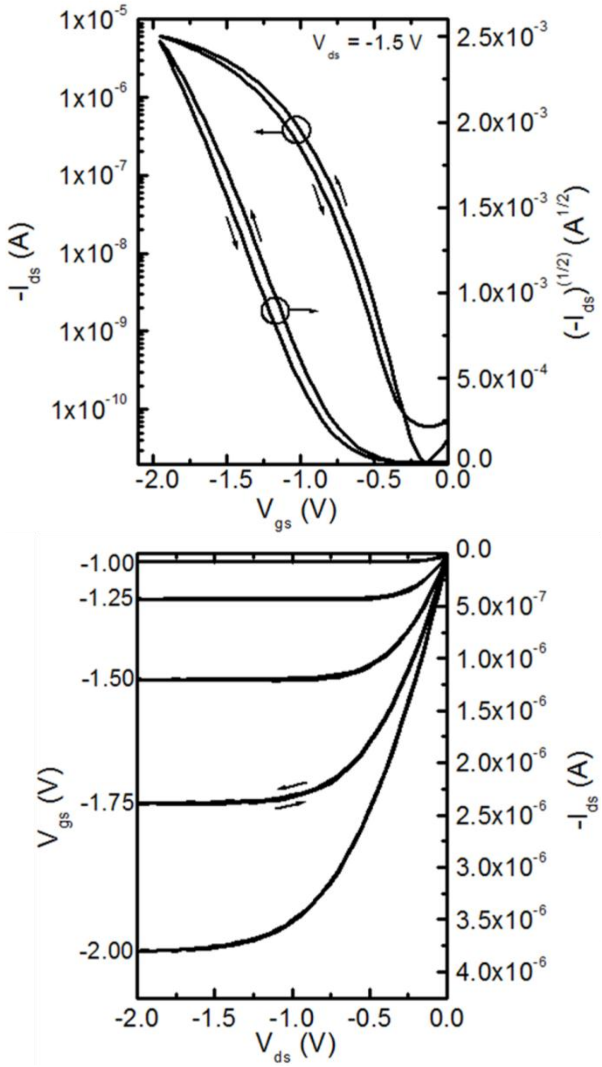

**Figure 14.** Characteristic transfer (A) and output curves (B) of top-contact pentacene FET devices made with ultra-thin hybrid SAM-oxide dielectric (W = 1000 µm L = 20 µm). PhO-19-PA SAM formed by spin casting, annealing at 140 °C for 10 min., and solvent cleaning.

### *Low-Voltage Pentacene OFETs*

To demonstrate the potential of this dielectric material in OTFTs, top-contact pentacene devices were fabricated. After construction of a hybrid dielectric using the ideal processing conditions, substrates were placed in a thermal evaporator and allowed to heat to 60°C to ensure optimal pentacene growth conditions. Segregated regions of pentacene were then evaporated onto the surface of the substrates at 0.2Å/s using shadow mask. Once the evaporation was complete substrate were allowed to cool back to room temperature. Top contact gold electrodes were evaporated at 1Å/s and patterned with shadow mask.

20 µm channel length pentacene devices were found to exhibit excellent low-voltage performance. For $V_{ds}$ and $V_{gs}$ $\leq$ 2 V, charge carrier mobiles of up to 1.1 $cm^2V^{-1}s^{-1}$, average $V_t$ of 0.82 V, average $S$ of 126.6 mV/dec, and $I_{on}/I_{off}$ ranging from $1.1x10^5$ to $1.0x10^6$ were observed (**Figure 14 & Table 4**). Additionally, minimal hysteresis is shown to exist in both output and transfer curves.

**Table 4.** Summary of pentacene FET device performance utilizing hybrid SAM-oxide dielectric layer. Twenty devices from two batches were measured, all with W = 1000 µm and L = 20 µm.

| $\mu$ ($cm^2 V^{-1} s^{-1}$) (High) Avg. ± St.Dev. | $V_t$ (V) Avg. ± St.Dev. | $S$ (mV/dec.) Avg. ± St.Dev. | $I_{on}/I_{off}$ (Range) |
|---|---|---|---|
| (1.1) 0.67 ± 0.24 | 0.82 ± 0.12 | 126.6 ± 33.2 | $1.1x10^5$-$1.0x10^6$ |

*Conclusions*

Ultra-thin hybrid dielectric structures utilizing SAMs and inorganic oxides result in highly functional components of OFET device architectures. Processing of molecularly complex SAMs capable of providing sufficient insulating properties can be achieved through rapid solid state annealing of spun cast bulk molecular films. This technique results in reduced solvent and compound requirements when compared with traditional wet processes. Solid state PhO-19-PA SAM densification was studied with AFM, XPS and NEXAFS. It was shown that PhO-19-PA SAM densification occurs rapidly at $T > T_m$ of the bulk film, with SAM density/order maximized at an annealing temperature of 140 °C. Surface carbon concentration of SAM covered substrate increases 9% (XPS) and SAM structure moves from a largely disordered state to ordered film with molecules tilted at 31° and 30° versus the surface normal for the alkyl chains and the phenyl rings, respectively (NEXAFS) after annealing at 140 °C. Dielectric properties corroborate spectroscopic/AFM measurements as leakage current drops from $10^{-5}$ to $7.7 \times 10^{-8}$ A/cm$^2$ at 3 V. Pentacene OTFT performance is demonstrated on this low-voltage platform with operating voltages of less than 2 V, and mobility of up to 1.1 cm$^2$ V$^{-1}$ s$^{-1}$.

### Spun Cast Self-Assembled Monolayer Field Effect Transistors

Due the synthetic flexibility of organic semiconductors, the active layer can be modified to meet various device constraints. This is exemplified in the pursuit of chemical sensors made from organic FETs; in which the semiconductor must be as thin as possible in order for adsorbed molecules to alter the electrical properties of the device.[73] One method of achieving such an architecture is through the use of self-assembled monolayer field effect transistors (SAMFETs) in which the semiconductor is comprised of a single molecular layer chemically adhered to the dielectric surface.

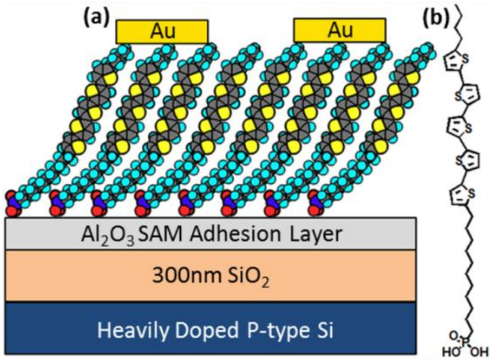

**Figure 15.** (a) SAMFET device architecture (cartoon). From bottom: P-doped Si with 300 nm oxide, 2 nm adhesion layer, BQT-PA, gold electrodes. (b) Chemical structure of BQT-PA.

In “Spun Cast Self Assembled Monolayer Field Effect Transistors,” published in Organic Electronics, top-contact self-assembled monolayer field-effect transistors (SAMFETs) were fabricated through both spin-coating and solution assembly of a semiconducting phosphonic acid-based molecule (11-(5""-Butyl-[2,2';5',2";5",2"';5"',2""]quinquethiophen-5-yl)undecylphosphonic acid) (BQT-PA). The field-effect mobilities of both spin-cast and solution assembled SAMFETs were 1.1 - 8.0 x $10^{-6}$ cm$^{2}$ V$^{-1}$ s$^{-1}$ for a wide range of channel lengths (between 12 and 80 µm). The molecular monolayers were characterized by atomic force microscopy (AFM), attenuated total reflectance-fourier transform infrared spectroscopy (ATR-FTIR), and near edge X-ray absorption fine structure (NEXAFS) spectroscopy. It was found that the BQT-PA monolayer films exhibit dense surface coverage, bidentate binding, and tilt angles of ~32° and ~44° for the thiophene rings and alkyl-chain, respectively. These results indicate that rapid throughput of fabricating SAMFETs is possible even by spin-coating.

The development of π-conjugated self-assembled monolayer (SAM) molecules has resulted in a new type of OFET; the self-assembled monolayer field effect transistor (SAMFET). Functionally, SAMFETs are OFETs in which the organic semiconductor is a single layer of well-packed π-conjugated molecules capable of acting as a charge-transporting channel. Fabrication of SAMFET devices has been attempted by several groups, however, most devices required channel lengths of less than 100 nm to ensure a gate voltage dependence of the source to drain channel current (apparently due to limited lateral interconnection of the semiconducting SAM).[74-76] Recently, SAMFETs with long channel lengths up to 40 µm have been demonstrated by Smits *et al.*, in which a SAM was formed on a silica gate dielectric via a greater than 15 h of immersion phase assembly.[77] Performance of these SAMFETs was comparable to that of OFETs constructed with a three-dimensional bulk film.

We demonstrate rapidly processed SAMFETs achieved through spin-coating a phosphonic acid-based molecule 11-(5""-Butyl-[2,2';5',2";5",2"';5"',2""]quinquethiophen-5-yl)undecylphosphonic acid (BQT-PA). The resulting spin-cast SAMs show uniform density, and well-ordered monolayer coverage comparable to that observed by conventional immersion phase solution assembly. The top-contact SAMFETs processed by spin-coating and immersion assembly show identical electronic performance.[52]

*Experimental*

BQT-PA was synthesized by Pd-catalyzed coupling between diethyl 11-(5'-bromo[2,2']bithiophen-5-yl)undecylphosphonate and (5''-butyl[2,2';5',2'']terthiophen-5-yl)trimethyltin at 90 $^{o}$C in toluene to afford diethyl BQT-phosphonate. By reacting with bromotrimethylsilane, the diethyl BQT-phosphonate was converted into ditrimethylsilyl BQT-phosphonate and then hydrolyzed to afford the target molecule BQT-PA. The architecture of the SAMFET device studied in this work is presented in **Fig. 15**. Heavily *p*-doped silicon substrates with a 300 nm thermal oxide layer were used as a gate and dielectric material. A thin (~2 nm) aluminum oxide ($Al_2O_3$) adhesion layer was formed via a plasma-enhanced deposition to promote the binding of the phosphonic acid headgroups. BQT-PA was assembled on the $Al_2O_3$ adhesion layer by either spin-coating at 3000 rpm from a 2 mM chloroform solution followed by a 10-minute of annealing at 140°C or by 16 h immersion assembly in a 0.1 mM chloroform solution. After either spin-coating or immersion assembly, SAM covered substrates were immersed in chlorobenzene held at 100 °C for 10 min, followed by spin rinsing with chlorobenzene to get rid of unbound molecules. All SAM processing occurred in a dry $N_2$

environment, followed by the thermal deposition of 50 nm thick gold to form source and drain electrodes to complete the top-contact SAMFETs.

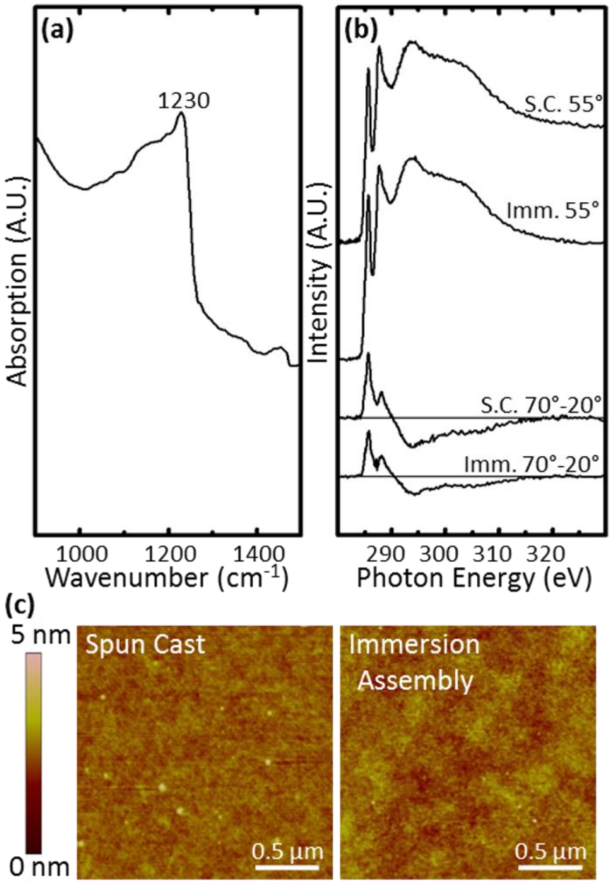

**Figure 16.** (a) ATR-FTIR spectra showing bidentate binding modes for BQT-PA. (b) NEXAFS data of both 55° and 70°-20° spectra for spin-cast (S.C.) and immersion assembly (Imm.) SAMs. (c) AFM image of spin-cast (left) and immersion assembled (right) SAM surface.

### *Atomic Force Microscopy*

The morphology of SAMs formed from both spin-coated and solution assembled samples were characterized by atomic force microscopy (AFM). They show that the active SAM layers are comprised of a single monolayer with minimal surface aggregate (**Fig. 16c**). Characterization of the SAM by attenuated total reflectance-fourier transform infrared spectroscopy (ATR-FTIR) was used to examine the binding mode of the molecule. Data in the $\nu_{PO}$ region shows the presence of $\nu_{P=O}$ stretching at 1230 $cm^{-1}$ as well as skeletal vibrations of phosphonate at 1110 $cm^{-1}$ (**Fig. 16a**). Due to the lack of well resolved $\nu_{P\text{-}O\text{-}H}$ vibrations at 900-1000 $cm^{-1}$, we infer that the phosphonate binding is predominantly bidentate.[9,10]

### *Near-Edge X-ray Absorption Fine Structure*

Near edge X-ray absorption fine structure (NEXAFS) spectroscopy can provide chemical identification of specific bonds within SAMs and detailed information about molecular alignment. **Fig. 16b** shows C K-edge spectra of BQT-PA SAMs collected at an X-ray incidence angle of $55^{\circ}$. At an incident angle of $55^{\circ}$, the spectra are independent of orientation effects (the so-called magic angle of NEXAFS). Within both spectra are characteristic absorption resonances at ~287.7 eV (R*/C-H σ*), and ~293.3 eV (C-C σ*) related to the aliphatic carbon chains and a feature at ~285.6 eV (C-C π*) related to the thiophene rings. In addition, no features related to contamination were present (i.e. a C=O related resonance near 288.5 eV). NEXAFS angle dependencies for both spin-coated and immersion-assembled, can be found in **Fig. 16b**. Both SAMs exhibit positive and negative dichroism for the R* and σ* resonances, respectively, indicating that the SAMs are oriented upright. Molecular orbitals related to the R* transition are oriented perpendicular to the alkyl chain axis while those related to transitions into the C-C and C-C’ σ* orbitals are orthogonally oriented parallel to the chain axis. The π* resonances exhibit pronounced positive dichroisms indicating the rings are orientated upright.

For a more quantitative analysis of these angle dependencies, the tilt angles with respect to the surface normal of the *n*-alkyl chains and the ring structures were determined from the dichroisms at the *R** and π* resonances, respectively. The intensities of these resonances as a function of the X-ray incidence angle are evaluated for the spectra taken at 70°, 55° and 20° using published procedures for vector orbitals.[61] From this data the average tilt angles for both spin-coated and immersion assembled SAMs were found to be 43.3 ± 5.0° and 44.0 ± 5.0° for the alkyl chain (R*/C-H σ*orbital) and 30.4 ± 5.0° and 34.2 ± 5.0° for the thiophene rings (C-C π* orbital), respectively.

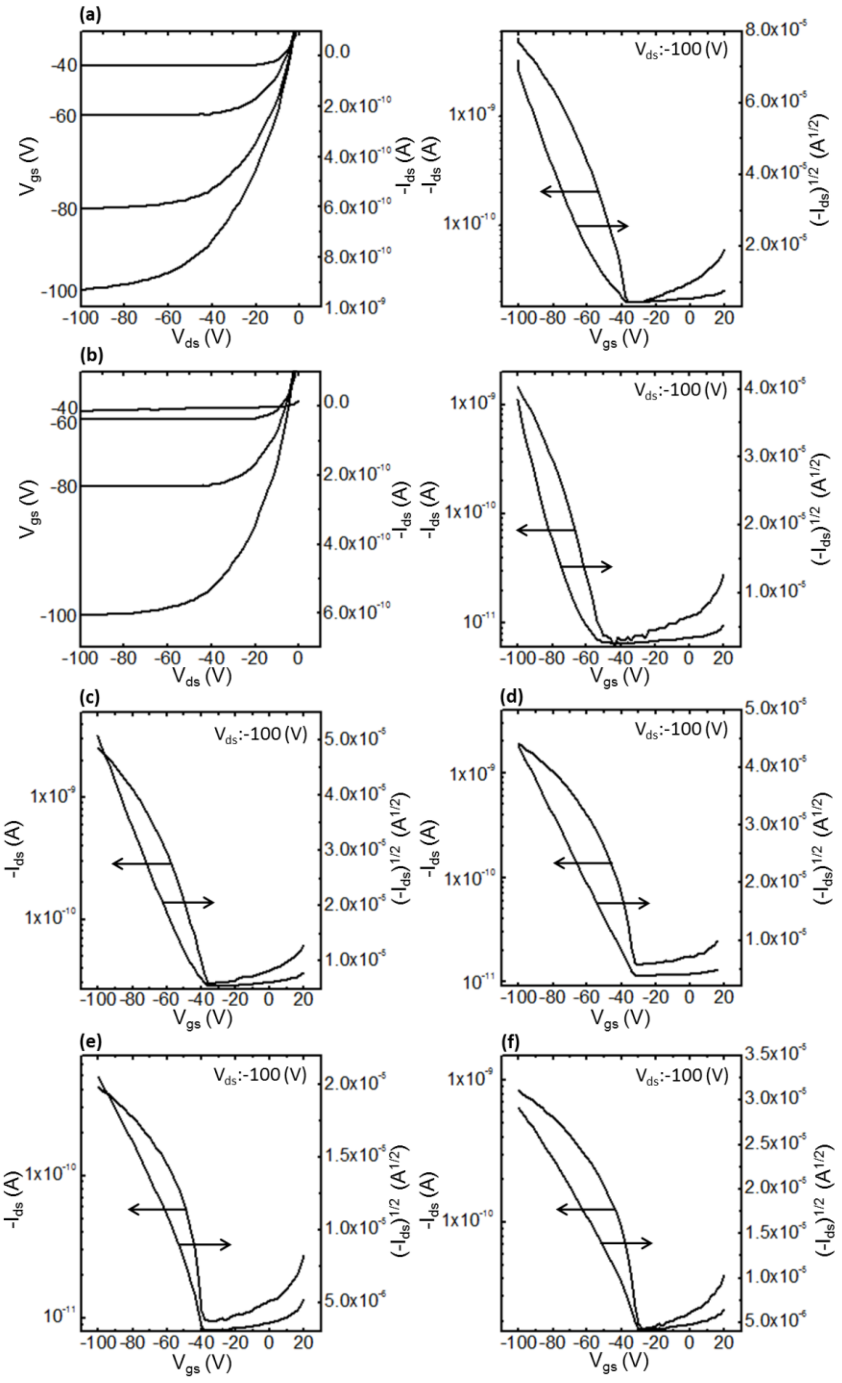

**Figure 17.** Representative output (left) and transfer (right) curves for (a) immersion assembled and (b) spin coated BQT-PA SAMFET devices (L = 12 μm, W = 1000 μm). (c-f) Spin coated SAMFET transfer curves (L = 20, 30, 50, 80 μm, respectively, W = 1000 μm).

**Table 5.** Comparison of high concentration (2mM BQT-PA in chlorobenzene) immersion assembled devices and identical spun cast devices. Charge carrier mobility (μ) and number of functional 12 μm channel length devices in the set.

| Channel Length (μm) | $\mu$ ($\times 10^{-6}$ cm$^2$ V$^{-1}$ s$^{-1}$) | $-V_t$ (V) | $I_{on}/I_{off}$ |
|---|---|---|---|
| 12 (Bulk) | 1.1 - 4.0 | 25 - 51 | (1.0 - 3.3) x10$^2$ |
| 12 (Imm) | 1.2 - 4.1 | 35 - 50 | (2.0 - 5.4) x10$^2$ |
| 12 (SC) | 1.3 - 8.0 | 32 - 53 | (1.0 - 5.6) x10$^2$ |
| 20 (SC) | 1.2 - 3.0 | 36 - 49 | (1.0 - 2.1) x10$^2$ |
| 30 (SC) | 1.7 - 2.1 | 30 - 48 | (1.1 - 3.0) x10$^2$ |
| 50 (SC) | 1.1 - 5.6 | 29 - 45 | (1.5 - 2.2) x10$^2$ |
| 80 (SC) | 1.1 - 4.0 | 31 - 42 | (0.9 - 1.0) x10$^2$ |

### *OFET Device Performance*

Top-contact SAMFET devices fabricated from the BQT-PA molecule demonstrated typical OFET output and transfer characteristics despite the active layer being comprised of only a single monolayer. Transistor characterization was performed in a $N_2$ environment using Agilent 4155B semiconductor parameter analyzer. The field effect mobility ($\mu$) was calculated in the saturation regime using a linear fit of $(-I_{ds})^{1/2}$ vs. $V_{gs}$. These devices were found to have an average $\mu$ of 1.1 - 8.0 x $10^{-6}$ cm$^2$ V$^{-1}$ s$^{-1}$ that was independent of channel length (device channel lengths measured were 12, 20, 30, 50 and 80 μm). $I_{on}/I_{off}$ current was on the order of $10^2$. This data was found to be consistent for both immersion-assembled and spin-coated devices, as both exhibited similar electronic properties.

Charge carrier mobility of our BQT-PA SAMFETs are comparable to those of SAMFETs based on a quarterthiophene phosphonic acid molecules.[78] However, the device performance still needs to be improved by further optimization of molecular design, processing and device structure. In future studies, we plan to tailor molecular moieties of the π-conjugated unit, alkyl chain and binding group to optimize molecular orientation and packing for efficient intermolecular electronic wavefunction overlap and source/drain electrode-SAM contact. Despite low $\mu$, we do not observe significant variation between spin-coated and immersion assembly processed devices for channel lengths from 12 to 80 μm. Therefore, spin-coating of semiconducting phosphonic acid molecules may provide a viable processing route for rapid throughput of SAMFETs.

### *Conclusion*

In conclusion, we have demonstrated a simple and generally applicable approach to fabricate SAMFETs through a rapid spin-coating process. Charge mobilities of 1.1 - 8.0 x $10^{-6}$ $cm^2$ $V^{-1}$ $s^{-1}$ were achieved for a wide range of channel lengths (from 12 to 80 μm). Characterization of the BQT-PA SAM was performed by AFM, ATR-FTIR, and NEXAFS, showing a densely packed monolayer with tilt angles of ~32° and ~44° for the thiophene rings and alkyl chains, respectively. This work is representative of major advancement in the processing of SAMFET devices, demonstrating that lengthy assembly procedures are not necessary to achieve high density SAMs capable of charge transport over long channel lengths.

**References:**

1. Shirakawa, H.; Louis, E. J.; MacDiarmid, A. G.; Chiang, C. K.; Heeger, A. J., *J. Am. Chem. Soc.* **1977**, 16, 578-580.

2. Lisong, Z.; Alfred, W.; Sheng-Chu, W.; Jie, S.; Sungkyu, P.; Thomas, N. J., *Appl. Phys. Lett.* **2006,** 88, 083502.

3. Sekitani, T.; Zschieschang, U.; Klauk, H.; Someya, T., *Nat. Mater.* **2010,** 9, 1015-1022.

4. Chamberlain, G. A., *Solar Cells* **1983,** 8, 47-83.

5. Marie, O. R., *SID Symposium Digest of Technical Papers.***2009,** 40, 600-602.

6. Dimitrakopoulos, C. D.; Malenfant, P. R. L., *Adv. Mater.* **2002,** 14, 99-117.

7. Forrest, S. R., **2004,** 428, (6986), 911-918.

8. Katz, H. E., *Chem. Mater.* **2004,** 16, 4748-4756.

9. Forrest, S.; Burrows, P.; Thompson, M., *Spectrum, IEEE* **2000,** 37, 29-34.

10. Muccini, M., *Nat. Mater.* **2006,** 5, (8), 605-613.

11. Coropceanu, V.; Cornil, J. r. m.; da Silva Filho, D. A.; Olivier, Y.; Silbey, R.; Bredas, J.-L., *Chem.Rev.***2007,** 107, 926-952.

12. Klauk, H., *Organic Electronics: Materials, Manufacturing and Applications*. Wiley-VCH: **2006**.

13. Kittel, C., In *Intoduction to Solid State Physics*, Johnson, S., Ed. John Wiley & Sons, Inc: Hoboken, NJ, **2005**.

14. Brunetti, F. G.; Gong, X.; Tong, M.; Heeger, A. J.; Wudl, F., *Angew.Chem. Int. Ed.* **2010** 49, 532-536.

15. Scott, J. C., *J. Vac. Sci. Technol. A.* **2003,** 21, 521-531.

16. Moliton, A.; Hiorns, R. C., *Polym. Int.* **2004,** 53, 1397-1412.

17. Ma, H.; Yip, H.-L.; Huang, F.; Jen, A. K. Y., **2010** 20, 1371-1388.

18. Newman, C. R.; Frisbie, C. D.; da Silva Filho, D. A.; Bredas, J.-L.; Ewbank, P. C.; Mann, K. R., *Chem. Mater.* **2004,** 16, 4436-4451.

19. Sanvito, S., *Nat. Mater.* **2007,** 6, 803-804.

20. Rogers, J. A.; Bao, Z.; Makhija, A.; Braun, P., *Adv. Mater.* **1999,** 11, 741-745.

21. Baek, N. S.; Hau, S. K.; Yip, H.-L.; Acton, O.; Chen, K.-S.; Jen, A. K. Y., *Chem. Mater.* **2008,** 20, 5734-5736.

22. DiBenedetto, S. A.; Facchetti, A.; Ratner, M. A.; Marks, T. J., *Advanced Materials* **2009,** 21, 1407-1433.

23. Gundlach, D. J., *Nat. Mater.* **2007,** 6, 173-174.

24. Houssa, M., *High-K Gate Dielectrics*. Institute of Physics: **2004**.

25. Katsouras, I.; Geskin, V.; Kronemeijer, A. J.; Blom, P. W. M.; de Leeuw, D. M., *Org. Electron.* **2011,** 12, 857-864.

26. Hulea, I. N.; Fratini, S.; Xie, H.; Mulder, C. L.; Iossad, N. N.; Rastelli, G.; Ciuchi, S.; Morpurgo, A. F., *Nat. Mater.* **2006,** 5, 982-986.

27. Giri, G.; Verploegen, E.; Mannsfeld, S. C. B.; Atahan-Evrenk, S.; Kim, D. H.; Lee, S. Y.; Becerril, H. A.; Aspuru-Guzik, A.; Toney, M. F.; Bao, Z., *Nature.* **2011,** 480, 504-508.

28. Briseno, A. L.; Mannsfeld, S. C. B.; Jenekhe, S. A.; Bao, Z.; Xia, Y., *Materials Today* **2008,** 11, 38-47.

29. Horowitz, G,. *Adv. Mater.* **1998,** 10, 365-377.

30. Acton, O.; Dubey, M.; Weidner, T.; O'Malley, K. M.; Kim, T.-W.; Ting, G. G.; Hutchins, D.; Baio, J. E.; Lovejoy, T. C.; Gage, A. H.; Castner, D. G.; Ma, H.; Jen, A. K. Y., *Adv. Funct.Mater.* **2011,** 21, 1476-1488.

31. Chua, L.-L.; Zaumseil, J.; Chang, J.-F.; Ou, E. C. W.; Ho, P. K. H.; Sirringhaus, H.; Friend, R. H., *Nature.* **2005,** 434, 194-199.

32. Kim, S.-J.; Ryu, K.; Chang, S., *J. Mater. Sci.***2010,** 45, 566-569.

33. Bain, C. D.; Whitesides, G. M., *Angew. Chem. Int.Ed.* **1989,** 28, 506-512.

34. Cheng, X.; Noh, Y.-Y.; Wang, J.; Tello, M.; Frisch, J.; Blum, R.-P.; Vollmer, A.; Rabe, J. P.; Koch, N.; Sirringhaus, H., *Adv. Funct. Mater.* **2009,** 19, 2407-2415.

35. Byoung Hun, L.; Laegu, K.; Renee, N.; Wen-Jie, Q.; Jack, C. L., *Appl. Phys. Lett.* **2000,** 76, 1926-1928.

36. Acton, O.; Ting Ii, G. G.; Ma, H.; Hutchins, D.; Wang, Y.; Purushothaman, B.; Anthony, J. E.; Jen, A. K. Y., *J. Mater.Chem.* **2009,** 19, 7929-7936.

37. Bain, C. D.; Troughton, E. B.; Tao, Y.-T.; Evall, J.; Whitesides, G. M., *J. Am. Chem. Soc.* **1989,** 111, 321-335.

38. Byloos, M.; Al-Maznai, H.; Morin, M., *J. Phys. Chem. B.* **1999,** 103, 6554-6561.

39. Ting, G. G.; Acton, O.; Ma, H.; Ka, J. W.; Jen, A. K. Y., *Langmuir*. **2009,** 25, 2140-2147.

40. Schwartz, D. K., *Annu. Rev. Phys. Chem.* **2001,** 52, 107-137.

41. Luschtinetz, R.; Oliveira, Augusto F.; Duarte, Hélio A.; Seifert, G., *Zeitschrift für anorganische und allgemeine Chem.* **2010,** 636, 1506-1512.

42. Kenjiro, F.; Takanori, H.; Tomoyuki, Y.; Tsuyoshi, S.; Ute, Z.; Hagen, K.; Takao, S., *Appl. Phys. Lett.* **2009,** 95, 203301.

43. Liao, K.-C.; Ismail, A. G.; Kreplak, L.; Schwartz, J.; Hill, I. G., *Adv. Mater*. **2010,** 22, 3081-3085.

44. Kelley, T. W.; Boardman, L. D.; Dunbar, T. D.; Muyres, D. V.; Pellerite, M. J.; Smith, T. P., *J. Phys.Chem.B.* **2003,** 107, 5877-5881.

45. Froehlich, H., *Theory of dielectrics: dielectric constant and dielectric loss*. Clarendon: Oxford, **1958**.

46. Lee, J.; Panzer, M. J.; He, Y.; Lodge, T. P.; Frisbie, C. D., *J. Am. Chem. Soc.***2007,** 129, 4532-4533.

47. Zhou, H.; Yang, L.; You, W., *Macromolecules,* **2012,** 45, 607-632.

48. Mikroyannidis, J. A.; Kabanakis, A. N.; Sharma, S. S.; Sharma, G. D., *Adv. Funct. Mater.* 21, 746-755.

49. Anthony, J. E.; Facchetti, A.; Heeney, M.; Marder, S. R.; Zhan, X., *Adv. Mater.* **2010,** 22, 3876-3892.

50. Riede, M.; Mueller, T.; Tress, W.; Schueppel, R.; Leo, K., *Nanotechnology* **2008,** 19, 424001.

51. Jun, W.; Bin, W.; Jianhua, Z., *Semicond. Sci. Technol.* **2008,** 23, 055003.

52. Hutchins, D. O.; Acton, O.; Weidner, T.; Cernetic, N.; Baio, J. E.; Ting, G.; Castner, D. G.; Ma, H.; Jen, A. K. Y., *Org. Electron.* **2012,** 13, 464-468.

53. Acton, O.; Hutchins, D.; Árnadóttir, L.; Weidner, T.; Cernetic, N.; Ting, G. G.; Kim, T.-W.; Castner, D. G.; Ma, H.; Jen, A. K. Y., *Adv. Mater.***2011,** 23, 1899-1902.

54. Briseno, A. L.; Aizenberg, J.; Han, Y.-J.; Penkala, R. A.; Moon, H.; Lovinger, A. J.; Kloc, C.; Bao, Z., *J. Am. Chem. Soc.* **2005,** 127, 12164-12165.

55. Yang, H.; Shin, T. J.; Ling, M.-M.; Cho, K.; Ryu, C. Y.; Bao, Z., *J. Am. Chem. Soc.* **2005,** 127, 11542-11543.

56. Don Park, Y.; Lim, J. A.; Lee, H. S.; Cho, K., Interface engineering in organic transistors. *Mater. Today*. **2007,** 10, 46-54.

57. Di, C.-a.; Yu, G.; Liu, Y.; Guo, Y.; Sun, X.; Zheng, J.; Wen, Y.; Wang, Y.; Wu, W.; Zhu, D., *Phys. Chem. Chem. Phys.***2009,** 11, 330.

58. Lee, H. S.; Kim, D. H.; Cho, J. H.; Hwang, M.; Jang, Y.; Cho, K., *J. Am. Chem. Soc.* **2008,** 130, 10556-10564.

59. Wang, C.-H.; Hsieh, C.-Y.; Hwang, J.-C., *Adv.Mater.* **2011,** 23, 1630-1634.

60. Wu, S., *J. Adhesion.* **1973,** 5, 39-55.

61. Stohr, J., *Nexafs Spectroscopy*. Springer-Verlag: **1992**.

62. Lee, C.-Y.; Gong, P.; Harbers, G. M.; Grainger, D. W.; Castner, D. G.; Gamble, L. J., *Anal.Chem.* **2006,** 78, 3316-3325.

63. Gundlach, D. J.; Lin, Y. Y.; Jackson, T. N.; Nelson, S. F.; Schlom, D. G., *Electron Device Letters, IEEE* **1997,** 18,, 87-89.

64. Acton, O.; Ting, G. G.; Shamberger, P. J.; Ohuchi, F. S.; Ma, H.; Jen, A. K. Y., *ACS Appl. Mater. Interfaces.* **2010,** 2, 511-520.

65. Halik, M.; Klauk, H.; Zschieschang, U.; Schmid, G.; Dehm, C.; Schutz, M.; Maisch, S.; Effenberger, F.; Brunnbauer, M.; Stellacci, F., *Nature.* **2004,** 431, 963-966.

66. Yeong Don, P.; Do Hwan, K.; Yunseok, J.; Minkyu, H.; Jung Ah, L.; Kilwon, C., *Appl. Phys. Lett.* **2005,** 87, 243509.

67. Vuillaume, D.; Boulas, C.; Collet, J.; Davidovits, J. V.; Rondelez, F., *Appl. Phys. Lett.* **1996,** 69, 1646-1648.

68. DiBenedetto, S. A.; Frattarelli, D.; Ratner, M. A.; Facchetti, A.; Marks, T. J., J. *Am. Chem. Soc.* **2008,** 130, 7528-7529.

69. Nie, H.-Y.; Walzak, M. J.; McIntyre, N. S., *J. Phys.Chem. B.* **2006,** 110, 21101-21108.

70. Jianwei, Z.; Kohei, U., *Applied Physics Letters* **2003,** 83, 2034-2036.

71. Frey, S.; Stadler, V.; Heister, K.; Eck, W.; Zharnikov, M.; Grunze, M.; Zeysing, B.; Terfort, A., *Langmuir*. **2001,** 17, 2408-2415.

72. Dubey, M.; Gouzman, I.; Bernasek, S. L.; Schwartz, J., *Langmuir*. **2006,** 22, 4649-4653.

73. Andringa, A.-M.; Spijkman, M.-J.; Smits, E. C. P.; Mathijssen, S. G. J.; Hal, P. A. v.; Setayesh, S.; Willard, N. P.; Borshchev, O. V.; Ponomarenko, S. A.; Blom, P. W. M.; de Leeuw, D. M., *Org. Electron.* **2010,** 11, 895-898.

74. Cao, Y.; Wei, Z.; Liu, S.; Gan, L.; Guo, X.; Xu, W.; Steigerwald, M. L.; Liu, Z.; Zhu, D., *Angew. Chem. Int. Ed.***2010,** 49, 6319-6323.

75. Tulevski, G. S.; Miao, Q.; Fukuto, M.; Abram, R.; Ocko, B.; Pindak, R.; Steigerwald, M. L.; Kagan, C. R.; Nuckolls, C., *J. Am. Chem. Soc.* **2004,** 126, 15048-15050.

76. Mottaghi, M.; Lang, P.; Rodriguez, F.; Rumyantseva, A.; Yassar, A.; Horowitz, G.; Lenfant, S.; Tondelier, D.; Vuillaume, D., *Adv. Funct. Mater.* **2007,** 17, 597-604.

77. Smits, E. C. P.; Mathijssen, S. G. J.; van Hal, P. A.; Setayesh, S.; Geuns, T. C. T.; Mutsaers, K. A. H. A.; Cantatore, E.; Wondergem, H. J.; Werzer, O.; Resel, R.; Kemerink, M.; Kirchmeyer, S.; Muzafarov, A. M.; Ponomarenko, S. A.; de Boer, B.; Blom, P. W. M.; de Leeuw, D. M., *Nature.* **2008,** 455, 956-959.

78. Novak, M.; Ebel, A.; Meyer-Friedrichsen, T.; Jedaa, A.; Vieweg, B. F.; Yang, G.; Voitchovsky, K.; Stellacci, F.; Spiecker, E.; Hirsch, A.; Halik, M., *Nano Lett.* **2011,** 11, 156-159.